

Contents lists available at [SciVerse ScienceDirect](http://SciVerse.ScienceDirect.com)

Journal of Theoretical Biology

journal homepage: www.elsevier.com/locate/jtbi

Cells as state machines: Cell behavior patterns arise during capillary formation as a function of BDNF and VEGF

Byron L. Long*, Rahul Rekhi, Amada Abrego, Jiwon Jung, Amina A. Qutub*

Department of Bioengineering, Rice University, 6100 Main St., Houston, TX 77005, USA

HIGHLIGHTS

- ▶ Endothelial cells have key behavior states regulated by BDNF and VEGF.
- ▶ The frequency and sequence of transitions in cell behaviors determine angiogenic sprouting.
- ▶ A Rules-as-Agents framework allows automated, rapid hypothesis testing.
- ▶ A genetic algorithm correlates cell decision-making to *in vitro* tissue level response.

ARTICLE INFO

Article history:

Received 20 April 2012

Received in revised form

17 October 2012

Accepted 28 November 2012

Keywords:

Angiogenesis

Agent-based modeling

Endothelial cell patterning

Capillary phenotypes

ABSTRACT

Cell behavior patterns that lead to distinct tissue or capillary phenotypes are difficult to identify using existing approaches. We present a strategy to characterize the form, frequency, magnitude and sequence of human endothelial cell activity when stimulated by vascular endothelial growth factor (VEGF) and brain-derived neurotrophic factor (BDNF). We introduce a “Rules-as-Agents” method for rapid comparison of cell behavior hypotheses to *in vitro* angiogenesis experiments. Endothelial cells are represented as machines that transition between finite behavior states, and their properties are explored by a search algorithm. We rank and quantify differences between competing hypotheses about cell behavior during the formation of unique capillary phenotypes. Results show the interaction of tip and stalk endothelial cells, and predict how migration, proliferation, branching, and elongation integrate to form capillary structures within a 3D matrix in the presence of varying VEGF and BDNF concentrations. This work offers the ability to understand – and ultimately control – human cell behavior at the microvasculature level.

© 2012 Elsevier Ltd. All rights reserved.

1. Introduction

Brain ischemia affects over 600,000 people in the U.S. annually, leading to strokes, vascular dementia, and neurodegeneration. Despite this, the only FDA approved drug for treating ischemic stroke is tissue plasminogen activator (tPA), which can only be given to a subset of patients. No drugs have been approved for vascular dementia. However, one possible strategy for treating patients with brain ischemia is improving blood flow through regeneration of the microvasculature, also known as therapeutic angiogenesis. One way to achieve therapeutic angiogenesis is by enhancing or mimicking endogenous capillary regrowth (Arai et al., 2009).

Endogenously, hypoxia or low oxygen stimulates angiogenesis by activating vascular cells of the brain and inducing the expression of chemokines that drive cell movement. In cerebral ischemia, activity of the transcription factor hypoxia-inducible factor 1 (HIF1) increases in viable tissue around an occlusion, causing increased glycolysis and upregulation of vascular endothelial growth factor (VEGF) (Fig. 1a). This results in a degree of neuroprotection and, potentially, neuroregeneration (Beck and Plate, 2009; Jin et al., 2000; Mu et al., 2003; Pichiule et al., 2003; Sun et al., 2003). VEGF and its receptors are just one protein family that can modify brain angiogenic and neurogenic activity during hypoxia. Many proteins that modulate endothelial cell growth and migration also have effects on neurons and *vice versa* (Carmeliet and Tessier-Lavigne, 2005; Mukoyama et al., 2002). These include brain-derived neurotrophic factor (BDNF), the Ang-Tie receptor family, nerve growth factor (NGF), fibroblast growth factor 2 (FGF2), delta-like 1 (Dll1) and Noggin. Studies have indicated a high degree of complex, temporal-specific angiogenic responses to signaling among different protein families.

* Corresponding authors at: Department of Bioengineering, Rice University, 6500 Main St., Suite 610, Houston, TX 77005, USA. Tel.: +1 925 353 8870.

E-mail addresses: bl6@rice.edu (B.L. Long), rahul.rekhi@rice.edu (R. Rekhi), amada.abrego@gmail.com (A. Abrego), jj9@rice.edu (J. Jung), aminaq@rice.edu (A.A. Qutub).

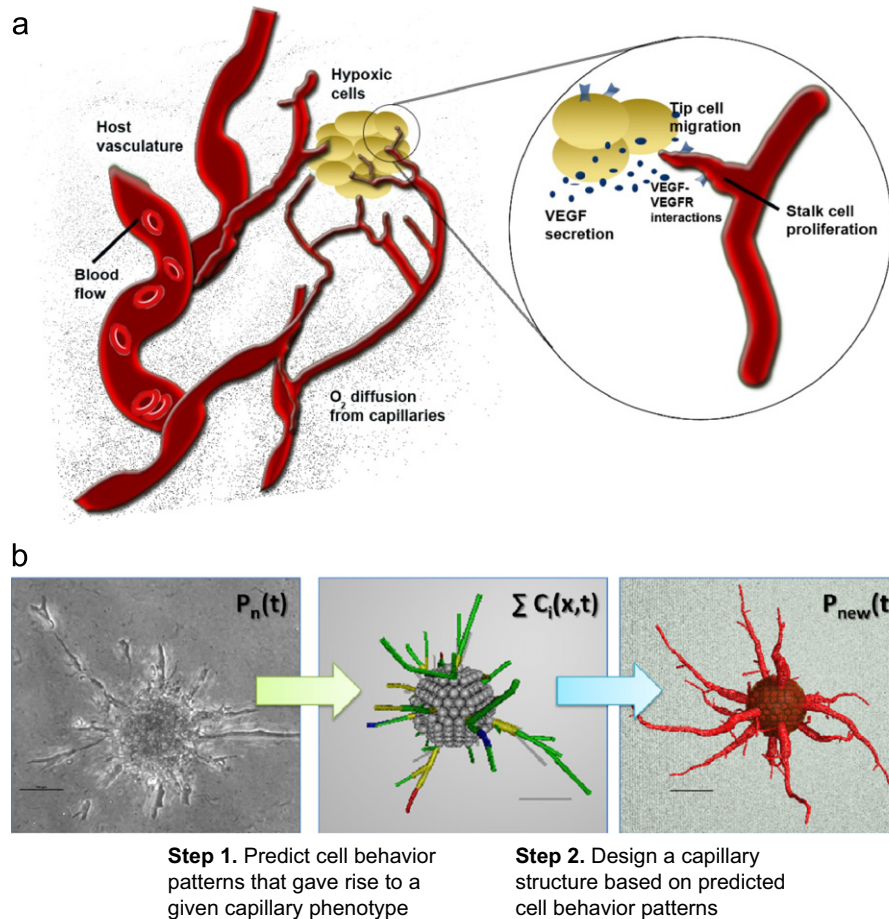


Fig. 1. Engineering angiogenesis. (a) During hypoxia, the upregulation of HIF1 induces hypoxic cells to secrete growth factors like VEGF and BDNF. Endothelial cells on adjacent vasculature become activated. Led by tip cells, activated cells migrate towards the growth factor source, proliferate and branch to form new capillaries; the developing capillary network may help replenish local oxygen supply. (b) From *in vitro* observations, a framework for controlling cell behavior can be created for producing capillary growth.

For example, in a rat brain model of ischemia–reperfusion injury, VEGF, VEGFR1, VEGFR2 and Ang2 levels peaked 1 day after injury, followed by Ang1 and Tie receptor expression peaking at day 3 post-injury; the latter time correlated with increased angiogenesis (Croll and Wiegand, 2001). Another study showed administration of VEGF after focal cerebral ischemia in rat produced an early neuroprotective affect, but showed angiogenesis after 7 days and neurogenesis only after 28 days (Sun et al., 2003). Notably, even in the same initial mechanical environment, differences in growth factors determine vessel structures (Poche et al., 2010). Growth factor levels are as critical as their timing (Manoonkitiwongsa et al., 2004). Sustained overexpression of BDNF, VEGF and FGF2 increases neurogenic activity through interconnected and independent pathways (Chen et al., 2007; Shi et al., 2009). Their associated genes are upregulated post-ischemia (Chen et al., 2007; Qu et al., 2007) and have recently been shown to crosstalk in stroke victims (Manso et al., 2012). However, detailed mechanisms of how neurovasculature forms as a function of these compounds have been difficult to study using existing techniques. Researchers in the field emphasize that we need significantly greater understanding of how cells of the human neurovasculature respond to HIF1 pathway proteins and angiogenic growth factors in order to design effective therapies for diseases like stroke (Harten et al., 2010; Lee et al., 2009; Ratan et al., 2007). Because of the multitude of cellular behaviors they can influence, quantitative modeling coupled with experiments becomes essential to understand how the complex dynamics of these angiogenic molecules correlate to cell behaviors. Our goal is to develop a

method to systematically and quantitatively study the effects of neurovascular growth factor combinations on cell behavior with the ultimate aim of being able to control angiogenic growth (Fig. 1b). To that end, we first applied our analysis to characterize how endothelial cells respond to combinations of two of these neurotrophic and angiogenic proteins, VEGF and BDNF.

We present an integrated computational–experimental strategy to test hypotheses as to what behaviors govern cell movement during vessel regeneration as a function of VEGF and BDNF stimulation. While most angiogenesis computational models represent the neovascularization process at the blood vessel level, a growing number of studies have explored individual cell behavior (Supplementary Table D.1). Of those that look at cell behavior, a handful specifically address how the different behaviors affect one another. For example, several studies have explored how Delta and Notch alter the proliferation and differentiation of tip and stalk cells, leading to fusion of tip cells and the lateral inhibition of tip cell phenotypes (Bentley et al., 2008, 2009; Jakobsson et al., 2010). Previously, we also showed how a specific sequence of cell behaviors led to capillary growth (Qutub and Popel, 2009) and other models have looked at the effects of contact inhibition (Merks et al., 2008) and cell elongation (Merks et al., 2006). While these models examine individual cell behaviors, they present only one hypothesis as to how behaviors affect one another. Here, we take a systems view of cell behavior and reanalyze assumptions about cell movement. Rather than assuming that the way cells interact with one another is known, we systematically test

Table 1
Migration equations.

Migration equations	
1.	Tip cell migration speed: Tip cell migration speed: $m = \min(m_{\text{baseline}} + m_{\text{chemotactic}}, \text{max}_{\text{migration}})$
2A.	Version A: Chemotactic component of tip cell migration speed: $m_{\text{chemotactic}}$ $m_{\text{chemotactic}} = m_{\text{baseline}} \times (c_1 \times [\text{VEGF}])$
2B.	Version B: Chemotactic component of tip cell migration speed: $m_{\text{chemotactic}}$ $\min_{\text{VEGF}} = e^{(100-c_3)/c_2}$ if $[\text{VEGF}] < \min_{\text{VEGF}}$ then $x_{\text{VEGF}} = 0$; otherwise $x_{\text{VEGF}} = ((c_2 \times \ln([\text{VEGF}]) + c_3)/100) - 1$ $m_{\text{chemotactic}} = m_{\text{baseline}} \times x_{\text{VEGF}}$
3.	Tip cell migration direction: $v = W_{\text{grad}} \times v_{\text{grad}} + W_{\text{pers}} \times v_{\text{pers}} + W_{\text{rand}} \times v_{\text{rand}}$ If this results in a change of direction of more than θ_{mig} then the weight of random component, w_{rand} , is reduced until the direction change is θ_{mig} .

Table 2
Proliferation equations.

Proliferation equations	
4A.	Version A (MPB, M2PB, MPMB) Cell growth: g $x_{\text{VEGF}} = r_1 \times [\text{VEGF}]$ If $[\text{BDNF}] \leq r_2$ then $x_{\text{BDNF}} = r_3$; otherwise $x_{\text{BDNF}} = r_4$ $g = \text{volume}_{\text{cell}} \times g_{\text{baseline}} \times (1 + x_{\text{VEGF}} + x_{\text{BDNF}})$
4B.	Version B (State Machine) Cell growth: g' $g' = g/n_{\text{active}}$ (g from equation 4A)
5.	Probability of mitosis: p $p = (l_{\text{prop}} \times r_5) + r_6$ Where l_{prop} is the length of the cell if its dimensions were in proportion

possibilities against experimental results. We then identify patterns in cell behavior that appear in response to stimuli. The computational framework and presented algorithms, coupled with the *in vitro* assays, provide a general strategy that could be used to explore single cell behavior during tissue formation, across cell and tissue types. Below, we introduce the justification and background for how we approached modeling and characterizing cell behavior.

2. Materials and methods

2.1. *In vitro* endothelial spheroid assay

We performed our *in vitro* analysis using the human umbilical vein endothelial cells (HUVEC) spheroid assay, based on published protocols (Korff and Augustin, 1998, 1999; Laib et al., 2009). Briefly, HUVEC (Lonza) were cultured in T75 flasks with EBM-2 media and bullet kit (Lonza) until confluent. Cells were trypsinized (0.05% Trypsin-EDTA, Sigma) and resuspended at 4×10^4 cells/ml into 20 μ l droplets. The droplets (hanging drops) were hung inverted on 50 mm petri dishes for 24 h. Approximately 400–500 cells were present in a 100 μ m diameter spheroid. We found that both the recommended 20% methocel (methylcellulose, Calbiochem) and 15% collagen (BD Bioscience) in media for the hanging drop worked for our assay. Simultaneously, we purchased the HUVEC angiogenic assay, licensed by Promocell (Heidelberg, Germany), from the Augustin lab. We choose the latter for our model comparisons shown in this paper, as the reproducibility and uniformity of the spheroid shape and initial size were optimized in the commercial assay. To these spheroids embedded in collagen, we added growth factors VEGF and BDNF (Sigma), diluted in endothelial cell media (EBM-2+bullet kit, Lonza). In each 24-well plate, we measured at minimum 10 spheroids per condition. We took phase contrast images (Nikon Ti-E microscope, 10 \times , 20 \times resolution) of the spheroids at 6 h, 24 h and 48 h. For our application of the model and genetic algorithm presented here, we focused on the 24 h *in vitro* time point. Measurements of overall angiogenic linear growth,

Table 3
Branching equations.

Branching equations	
6.	Cell branching probability: p If $[\text{VEGF}] > b_1$ or $[\text{BDNF}] > b_2$ then $p = b_3$; otherwise $p = b_4$

Table 4
Activation and morphological equations.

Activation and morphological equations	
7.	Cluster cell activation probability: p $p_{\text{VEGF}} = \min(1, \max(0, (\text{act}_{\text{VEGF}25} - \text{act}_{\text{VEGF}0})/25))$ $p_{\text{BDNF}} = \min(1, \max(0, (\text{act}_{\text{BDNF}50} - \text{act}_{\text{BDNF}0})/50))$ $p = 1 - ((1 - p_{\text{VEGF}}) \times (1 - p_{\text{BDNF}}))$
8.	Cell length-to-width-ratio: q $d = \text{distance from cell to tip cell in number of cells}$ if $d > q_{\text{dist}}$ then $q = q_{\text{min}}$; otherwise $q = q_{\text{max}} - ((q_{\text{max}} - q_{\text{min}}) \times d/q_{\text{dist}})$

calculation of branches, and branch lengths were performed in the Nikon image software program NIS Elements.

2.2. Cell model

Our computational models were developed using agent-based techniques. Agents represent endothelial cells. These virtual cells are analogous to adaptive robots: they can grow, divide, inherit properties, and change their behaviors as a function of their environment (Bonabeau, 2002; Maes, 1994). From the combinatorial interactions of single cells, complex capillary structures emerge (Bailey et al., 2007; Das et al., 2010; Liu et al., 2011; Qutub and Popel, 2009; Thorne et al., 2007). While agent-based microvasculature models have been applied diversely (Artel et al., 2011; Bailey et al., 2009; Jakobsson et al., 2010; Qutub and Popel, 2009) (Supplementary Table D.1), the commonality of the models lies in their ability to define cell behavior and molecular events through the use of rules. Rules are hypotheses based on published literature data, providing the instructions that guide an agent's activity. We first derived rules governing three endothelial cell behaviors (migration, proliferation and branching) from *in vitro* data obtained by a literature search, and subsequently compared the model results to our own spheroid assays (Tables 1–4, Supplementary Fig. C.1, Supplementary Tables D.2–D.5).

During angiogenesis, endothelial cells on quiescent vasculature become activated by stimuli such as VEGF or BDNF, and migrate towards higher growth factor concentrations. Sprouting angiogenesis also involves cell elongation and proliferation. To construct our initial cell behavior rules from literature, we chose two of the most prevalent angiogenic assays: *in vitro* 2D proliferation and migration assays. Proliferation and migration are main cellular events that drive vessel growth, and these 2D

assays can be high-throughput in nature, making them popular first screens for drug candidates that target angiogenesis (Staton et al., 2009). While there is one commonly used form of the 2D proliferation assay, there are two standard *in vitro* migration assays that we used to build the model: the scratch assay and the Boyden chamber assay. The Boyden chamber assay measures cell migration across a semi-permeable membrane towards growth factor stimuli in solution on the other side of the membrane while the scratch assay measures cell migration across a scratch or gap in a cell monolayer. These migration assays quantify the effects of changing stimuli (e.g., a growth factor gradient) on cell motility. After identifying cell behaviors of interest to develop the rules, we defined their form computationally and described how the rules interact with each other. We also setup initial model conditions to parallel the *in vitro* assays.

In this paper, we present on our three-dimensional, discrete time, agent-based model of endothelial cells forming angiogenic sprouts in response to varying concentrations of VEGF and BDNF in their microenvironment. Chains of endothelial cells sprout from a cluster of cells (a spheroid) and subsequently migrate, elongate, proliferate, and branch. At each time-step, cells act in a randomly determined order. Rules for behaviors were created from experimental observations relating each cell action to its local concentrations of VEGF and BDNF and physical properties. Migration rules specify the magnitude and direction of cell movement. Similarly, the proliferation rule defines the relative amount of cell volume increase. The branching rule determines if a branch will form and the orientation of the new branch cell. Below, we describe the details of the model and the rules for cell behaviors. Parameter values and their justification are provided in Supplementary Tables D.1–D.5.

2.2.1. Set up

The model starts with a cluster of spherical endothelial cells each of diameter d_{sphere} packed into a sphere of diameter d_{spheroid} (Korff and Augustin, 1998). These cells are packed in a face-centered cubic arrangement (Conway and Sloane, 1999) as shown in Fig. 2a and b.

2.2.2. Activation

Cells placed at the start of the simulation are in an inactive, dormant state. At each time-step, each inactive cluster cell is allowed to stochastically activate and become angiogenic. While the influence of VEGF on cell activation has been observed (McLaughlin and De Vries, 2001), we posit a similar, but lesser, effect for BDNF. The probability that a cell becomes active is a function of the cell's local VEGF and BDNF levels according to Equation 7. Cells that become active permanently laterally inhibit other cells within a r_{inhibit} cell neighborhood around them from becoming active. This inhibition prevents all cells from starting sprouts (Hellstrom et al., 2007). During activation, a cluster cell

creates a pair of sprouting stalk and tip cells of lengths len_{tip} and len_{stalk} and radius r_{init} and places them along the line passing through the cluster's center and the cell's center. Sprout cells are represented as sequences of one or more cylinders (see Fig. 2c). Each cylinder of a cell has the same radius, but different cells in the same sprout may have different radii.

2.2.3. Sprout cell shape

A sprout takes on a tapered shape as it grows. The cylinders of a tip cell have the maximum length-to-diameter ratio, q_{max} (Yu et al., 1997). The cylinders of stalk cells have uniformly decreasing length-to-diameter ratios according to their distance from the tip cell as measured in number of cells (Equation 8). However all stalk cells at or beyond a distance of q_{dist} cells from the tip cell have a length-to-diameter ratio of q_{min} . A cell attempts to achieve its length-to-diameter ratio after creating a new branch or increasing its volume, but before undergoing division (see Fig. 3). A cell meets its length-to-diameter ratio by changing its length and radius with three restrictions: (1) a cell's length cannot decrease; (2) a cell's radius cannot become greater than the radius of a sprout cell immediately behind it; and (3) a cell's radius cannot become less than the radius of a sprout cell immediately ahead of it.

2.2.4. Sprout connectivity and movement

Sprout cells are connected to each other in a single-file, end-to-end manner. The front of each cell is joined to the rear of the cell ahead of it. The leading tip cell of each sprout determines the path of all cells in its sprout, and sprout movement is similar to that of an eel's body led by its head. It is known that endothelial cells adhere to one another (Alberts et al., 2002) and that they can be stretched by external forces (Chang et al., 2003). Our model of tip cell migration thus includes elongation of the tip cell itself and the tip cell's immediately adjacent stalk cell. As such, the distance that a tip cell migrates can be restricted by the amount that it and the stalk cell behind it can stretch.

When a tip cell migrates, it first stretches to span the desired distance. The amount that a cell can elongate is determined by first calculating, from its current volume, the length necessary to attain its length-to-diameter ratio as estimated by endothelial cell measurements (Supplementary Table D.5). This distance is then increased by the factor e (Wang et al., 2003), yielding the maximum possible length of the cell. The difference between this maximum possible length and the tip cell's current length is the distance that it can elongate. If the tip cell attempts to move farther than it can elongate, it then tries to continue migrating by elongating the stalk cell immediately behind it. Any additional distance that the tip cell can migrate is then limited by the distance that the adjoining stalk cell can elongate. No other stalk cells can change during tip cell migration. Note that a stalk cell is

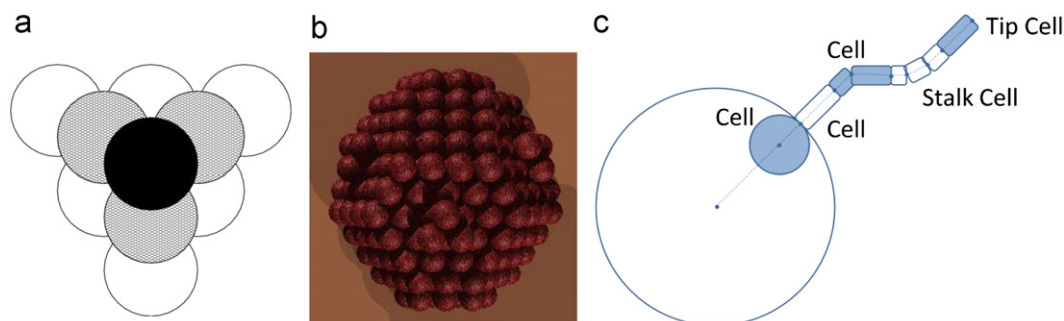


Fig. 2. Cell model. (a) Three partial layers of spheres packed in a face-centered cubic lattice. (b) A cluster of spherical cells packed into a larger sphere. (c) An initial activated cell in the spheroid and four cell agents in alternating shading sprouting from it. Initial placement and orientation of stalk and tip cell agents are determined by the centers of the cluster and the initial cell agent. Cell agents may have different radii, but each cylinder segment of a cell agent has the same radius.

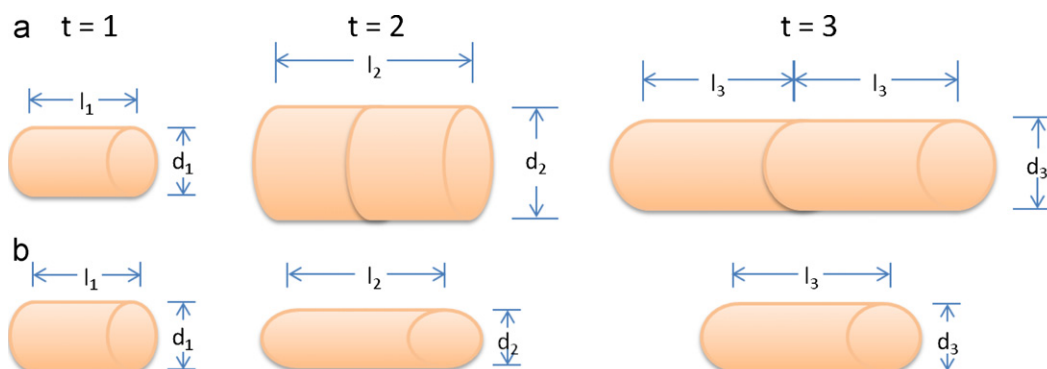


Fig. 3. Cell dimensions. (a) A growing cell changes its dimensions such that $l_1/d_1 = l_2/d_2$ and undergoes mitosis. In the next time-step, the newly divided cells change shape and share the original length to diameter ratio: $l_1/d_1 = l_3/d_3$. (b) An elongating cell reduces its diameter ($l_2 > l_1$, $d_2 < d_1$), and when later increasing in volume, moves towards its preferred dimensions without shortening its length ($l_3 = l_2$, $d_3 > d_2$).

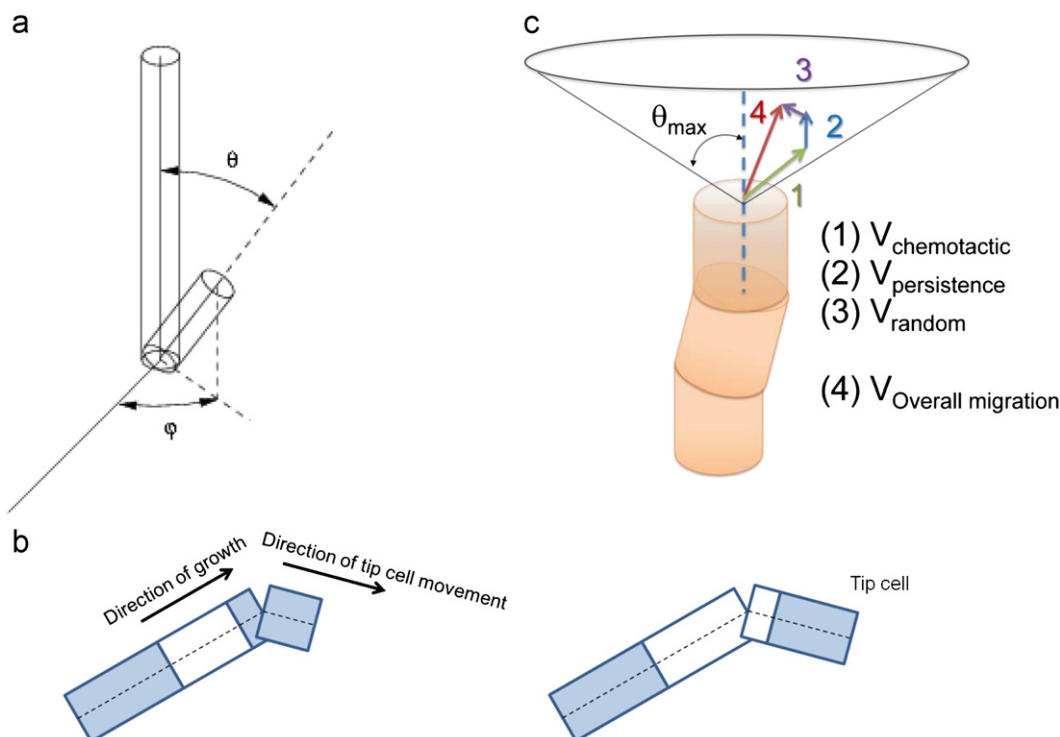


Fig. 4. Directional changes in the model. (a) A new cell shares endpoints with the cell from which it branches. Its orientation is determined by the angles θ and φ . (b) During proliferation (left), a white stalk cell will push its tip cell forward. After proliferation (right) the tip cell's length is unchanged and its front maintains its orientation. (c) Migration: Migration must be within θ_{\max} of the forward direction of a tip cell. The actual migration direction (arrow 4) is computed from a gradient, a vector in the forward direction, and a vector in a random direction.

not allowed to elongate at all if its front end forms a junction with two other cells (via branching) instead of just one tip cell.

The direction that a tip cell migrates is determined by three unit vectors. The first is a persistence vector that represents the tip cell's inertia (Harms et al., 2005). The second vector is determined by the VEGF gradient sensed by the front of the tip cell. The angle formed by the gradient and the persistence vector can be at most θ_{\max} (currently parameterized to prevent backwards migration). If the angle is greater than θ_{\max} , then a replacement for the gradient is selected among those vectors that point to the greatest change of VEGF concentration while being within θ_{\max} of the persistence vector. The third vector has its direction randomly selected and is used to represent nonuniform conditions not explicitly modeled. The results of weighting these vectors by w_{pers} , w_{grad} , and w_{rand} , respectively are summed (Equation 3) to determine the migration direction of the tip cell. If the sum is not within θ_{\max} of the persistence vector, then the random vector is reduced in magnitude until the sum is within θ_{\max} . See Fig. 4a.

A change in a cell's direction results in the creation of a new cylinder oriented in the direction change.

The magnitude of cell migration is computed from a baseline distance (Korff and Augustin, 1999; Rupp et al., 2004) and adjusted for the tip cell's local VEGF concentration (Equation 1). Two rules have been created reflecting the results of the Boyden chamber assay and the scratch assay. We derived the first rule using a linear regression of Boyden chamber data (Nakashio et al., 2002; Noiri et al., 1998; Wilson et al., 2006; Yamaguchi et al., 1999). Scratch assay data (Dimmeler et al., 2000) was used to construct Supplementary Fig. C.1a yielding the parameters c_2 and c_3 (Equation 2B). For both migration rules, the maximum distance is limited (Stokes et al., 1991).

2.2.5. Sprout cell proliferation

A sprout cell proliferates by increasing in volume. The rate of volume increase is derived from an extrapolation of cell count

assays (Varma et al., 2005). This volume increase is accounted for by a change in radius, length, or both. If the length of a tip cell increases, then the tip cell moves forward by increasing the length of its front-most cylinder. Hence a tip cell grows forward with no change in direction. A stalk cell's volume increase is limited by the existence of branches ahead of it in the sprout. If there is a branch ahead of the stalk cell, then it is assumed that the stalk cell is unable to push the entire structure forward. In such cases, the cell's volume increase is limited to a radial increase. When a stalk cell's length does increase, it pushes the cells ahead of it forward without compression as in Fig. 4b. The length increase is ultimately manifested as the tip cell moving in the direction of the main axis of its front cylinder distance equivalent to the length by which the original stalk cell increased.

If there is no branch ahead of a stalk cell, then after a volume increase, the cell may divide into two cells. Division is stochastic, and is more probable as the cell's volume increases. The length of the cell at its desired length-to-width ratio is used as a proxy for volume. Only if its length is at least len_{min} , can the cell divide with the probability given in Equation 5 (Neufeld et al., 1986). A cell divides across its main axis by evenly splitting at its length midpoint.

We determined the effect of VEGF on cell proliferation by performing linear regression of proliferation data (McLaughlin and De Vries, 2001; Wilson et al., 2006; Wu et al., 2006, 2000) (Supplementary Fig. C.1d).

2.2.6. Sprout cell branching

When a branch can be formed, the probability of a cell branching is a function of the cell's local VEGF and BDNF levels (Equation 6). A cell cannot form a branch at a point where one already exists. Branching is a total volume preserving action, and the volume of a new branch cell is taken from the volume of the cell from which it branches. The original cell and the new branch cell share their rearmost locations. The original cell remains on the sprout and the new branch cell extends away from it. In order to orient the new branch cell, two angles are required. The first is the angle of declination which is measured between the axis of the original cell's rearmost cylinder and the axis of the new branch cell's cylinder. It is randomly chosen between θ_{min} and θ_{max} . The second is the azimuth and is selected at random between 0° and 360° (see Fig. 4c). A new branch is started with a single cell of one cylinder of length l_b and radius r_b .

In both the constant-action (see Section 2.2.8) and state machine models (Section 2.2.9), newly created branches receive a boost in proliferation. This affects all cells along newly created branches in both types of models for a period of t_{branch} hours. For constant-action models, the proliferation volume of any cell in the branch is scaled by a factor of f_{branch} . For state machine models, the proliferation volume is unchanged, but the frequency of reaching the branching state is increased in two situations. First, when a cell on a branch reaches the idle state, it is instead immediately redirected to the proliferation state with a probability of p_{branch} . Second, if a tip cell is the only cell on a branch, then it is forced to its proliferation state whenever it attempts to make a transition to its migration state.

2.2.7. Time-step & transition time between events

Time-steps are 1 h intervals. We considered choosing the time interval between events in the state machine model one of three ways: mapping event to cell cycle and performing PI/BrdU assays over time, observing event changes by time-lapse videos, and allowing a search algorithm to choose times for us. In the end, we stayed with observations from live-cell imaging. Our choice of time interval length aligns with the 1 h interval used for

measuring the baseline net migration speed for endothelial cells (Rupp et al., 2004).

2.2.8. Constant-action models

In the constant-action models, each rule is applied at each time-step in a predetermined sequence (Fig. 5b). We tested three different constant-action models. The M-P-B model has each cell migrate (M), proliferate (P), and branch (B), in that order. The M-P-B model's migration rule was derived from experimental data based on the Boyden chamber assay. The M2-P-B model also has each cell migrate, proliferate, and then branch, but its migration rule was based on experimental data derived from the scratch assay. The M-P-M-B model uses the sequence: migrate, proliferate, migrate, branch, where the migration rule is derived from the Boyden chamber assay but is at half the usual magnitude of distance in each application.

2.2.9. State machine models

A state machine is defined by a finite set of states and a corresponding set of state-to-state transitions (Fig. 5d). These transitions control the sequence of states that a state machine may assume. Our state machine model is comprised of two separate state machines—one for tip cells and another for stalk cells (Supplementary Fig. C.2). Each basic endothelial cell behavior (i.e., migration proliferation branching elongation) is represented by a single state. In addition, we introduce an idle state for all cells which allows a cell to take no action during a time-step. Each transition is associated with a probability of the cell changing from one state to the other. A cell behaves as follows: when a cell is in a given state during a time-step, it randomly decides on a new state according to the probabilities of transitions from its current state. After a specific transition is selected, the cell performs the behavior and assumes its new state. Note that there are no transitions from a stalk cell state to the elongation state. Instead, the elongation state is synchronized with the tip cell's migration state. When a tip cell reaches the migration state, its adjacent stalk cell is forced into its elongation state (see Section 2.2.4). Each cell stores its own current state, and, with the exception of the case of elongation, each cell chooses its transition independently of other cells.

We assume that scratch and Boyden chamber assays of cell migration detect and measure only those cells that actually migrate, i.e., a derivation of a migration rate from these assays can exclude cells that did not migrate. Thus our state machine models can reuse the migration rules. The scratch assay migration rule was used by all state machine models considered. For proliferation, we assumed that a fixed percentage of cells at any moment are actively increasing in volume and that this increase is assigned to the entire population. This allows the cell volume increase computed by the proliferation rule to be adjusted by a constant factor when used by state machine models. The baseline migration rates (without growth factors) were estimated for migration in three-dimensions, and then the relative change in migration based on the scratch and Boyden chamber *in vitro* assays was extrapolated to consider migration with growth factor stimulation.

The basic state machines with transition probabilities as used here produce behavior that can be characterized as a Markov chain (Grinstead and Snell, 1997). Our focus on state machines reflects our initial view of cell control, and our adaptations are done at this level. Hence we are free to alter them in ways that do not adhere to the definition of a Markov chain. The use of a genetic algorithm to find transition probabilities (see Section 2.3) is consistent with this in that it makes no assumptions on the structure of our state machines. As a case in point, we have

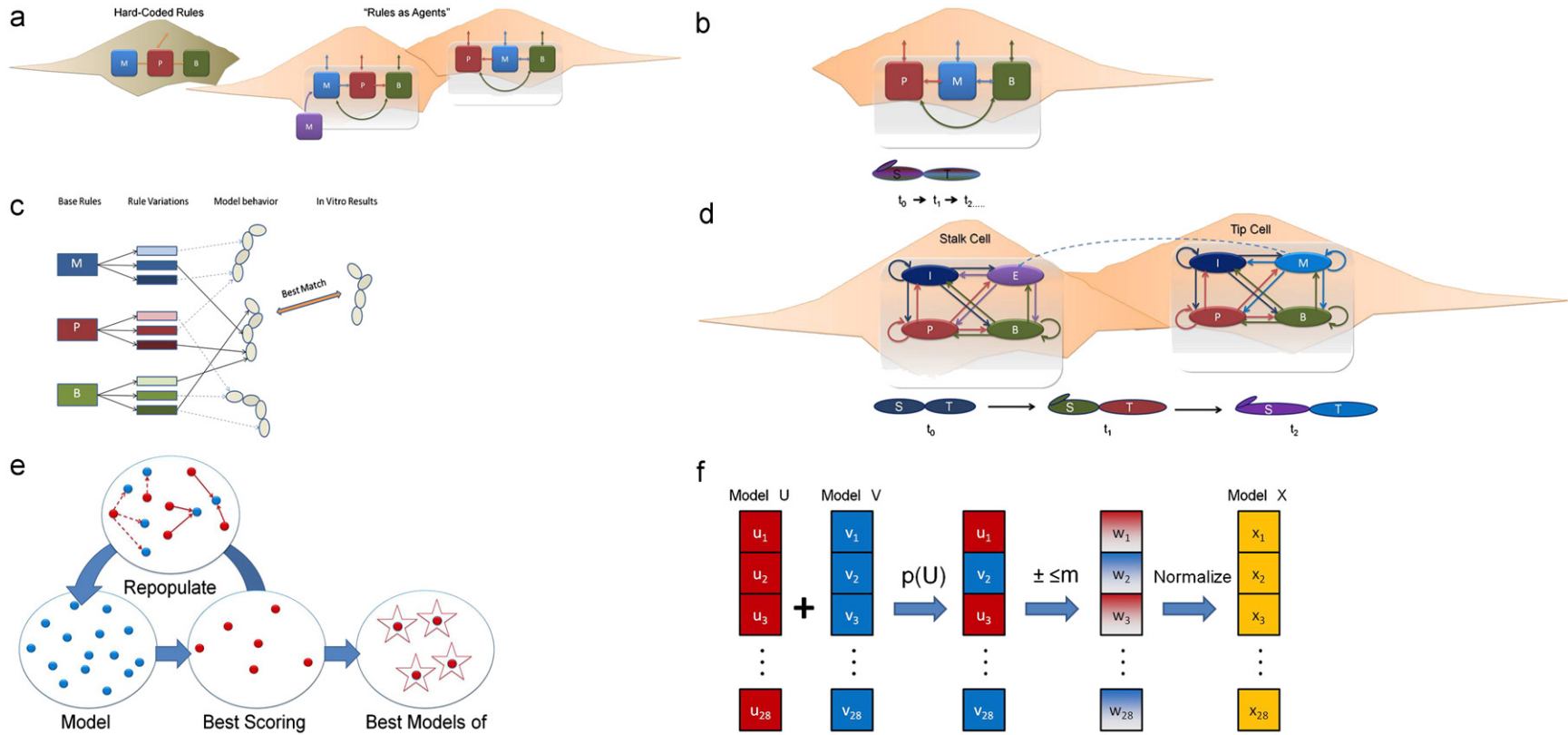


Fig. 5. Modeling cell behavior control. (a) Traditional agent-based models have rules (cell behaviors) hard-coded into the definition of a cell (gray cell). Rules as agents (tan cells) are modularized and separated from the cells. With the rule-oriented approach, rules can be rapidly replaced without extensive changes. Additionally, the rules can be tested and shared across labs or models. *M*=migration, *P*=proliferation, *B*=branching. (b) Original rule-oriented model where all cell behaviors are performed during a single time-step. (c) Schematic illustrating how the rule-oriented approach allows comparison of multiple sets of rules (hypotheses about cell behaviors) with experimental results. (d) Edges are labeled with transition probabilities in a state machine representation of a tip cell. Tip cell migration includes stalk cell elongation in both the original and state machine model. *P*=proliferation, *M*=migration, *B*=branching, *I*=idle, *E*=elongation. (e) Genetic algorithm steps: a set of models is generated (blue); the models' output is compared to *in vitro* data and the models that best match experiments are selected (red); from a set of top models, a new generation of models is produced through "cloning" (dashed arrows) or "sexual reproduction" (solid arrows). The process is iterated until an optimal matching model or sets of models are found. (f) "Sexual reproduction," involves parent models (*U* and *V*) passing on their features (u_n, v_n) to the next generation of models (*X*), with a mutation factor (m). (For interpretation of the references to color in this figure legend, the reader is referred to the web version of this article.)

altered how our state machine handles branching by allowing different behavior on a branch for a parameterized number of time-steps (see Appendix A). We made this change directly to the model without changing the number of states, and then immediately proceeded with a search for appropriate transition probabilities.

2.2.10. Rules-as-agents framework allows rapid hypothesis testing

One reason agent-based modeling is a flexible, attractive approach for modeling biological systems is that rules can take any form, including algebraic equations, differential equations, and propositional logic statements. The varied ways rules can be defined make it challenging to systematically compare agent-based models. More recently, parameter searches have been employed to optimize agent-based models (Ropella and Hunt, 2010), and results of parameterized models have been compared iteratively with experiments (Engelberg et al., 2011; Sheikh-Bahaei and Hunt, 2011). We advance this by allowing the form, frequency and sequence of cell behaviors to be rapidly exchanged, through development of the “Rules-as-Agents” (RAA) approach (Fig. 5a). In the RAA framework, rules themselves are agents and independent from the agents that they control. The framework also provides flexibility and modularity that allow candidate rules to be interchanged in order to discover rule combinations that better predict *in vitro* growth (Fig. 5c).

Our first application of the RAA framework was to test out the two different hypotheses for cell migration derived from Boyden chamber and scratch assays and the effect of different sequences

of cell behaviors. In addition, each individual rule was used by both the constant-action models and the state machine models.

2.3. Genetic algorithm searches for optimal transition probabilities

The reuse of individual rules from the constant-action models leaves transition probabilities to be determined for a state machine model. We determine transition probabilities by searching for a set of probabilities that result in model behavior that best matches the *in vitro* measurements of total sprout length, branch count, and average branch length. We use a genetic algorithm to accomplish this. Each possible state machine model is represented as a vector of transition probabilities. The genetic algorithm scored each model by first simulating it 20 times in each of 6 initial conditions: 0 ng/ml VEGF and 0 ng/ml BDNF; 0 ng/ml VEGF and 50 ng/ml BDNF; 0 ng/ml VEGF and 100 ng/ml BDNF; 25 ng/ml VEGF and 25 ng/ml BDNF; 25 ng/ml VEGF and 50 ng/ml BDNF; and 50 ng/ml VEGF and 0 ng/ml BDNF. The simulation results were converted to a model score by comparing 18 values (the average total sprout lengths, branch counts, and branch lengths for each initial condition) to measurements from the *in vitro* assays. The score for a model is the 18-dimensional distance (in units of standard deviations) between the model results and *in vitro* results:

$$(*) \quad \text{score}(\vec{a}) = \sqrt{\sum_{i \in I} \sum_{m \in M} \left(\frac{a_{i,m} - v_{i,m}}{\sigma_{i,m}} \right)^2}$$

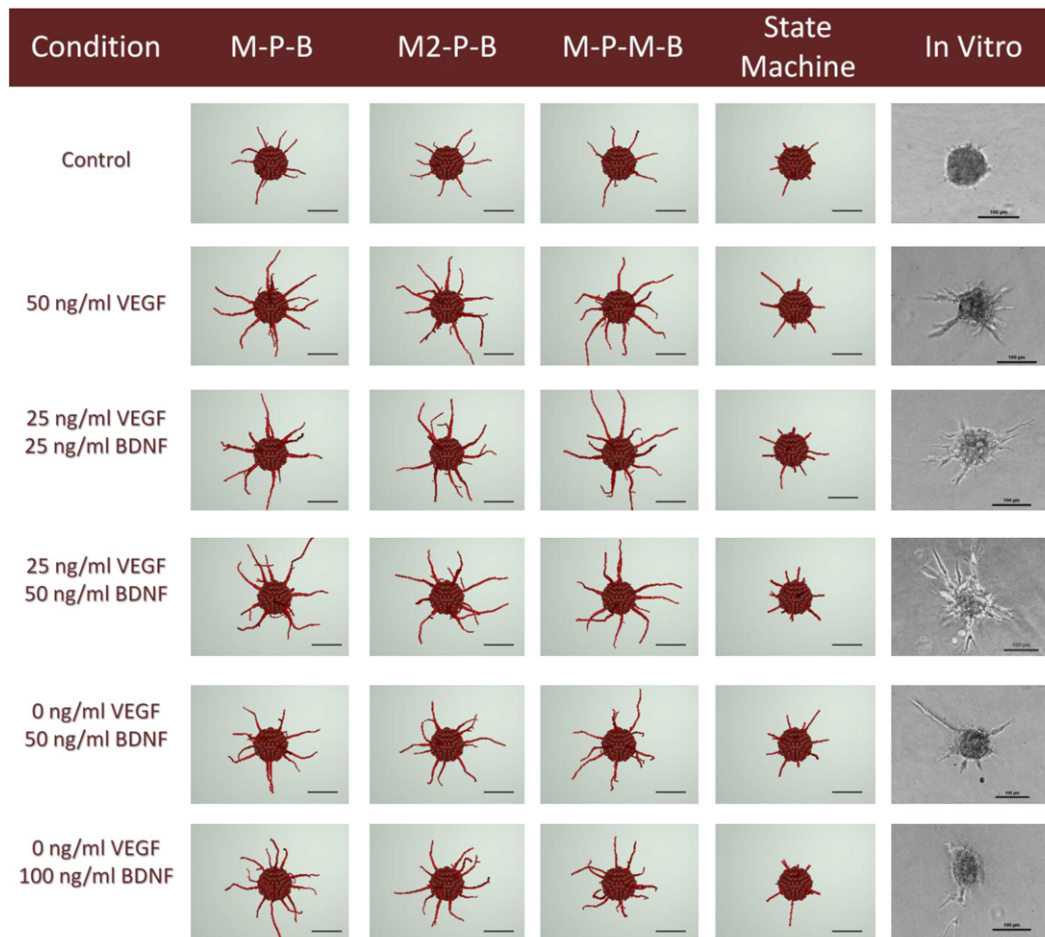


Fig. 6. Comparison of selected simulation results for the M-P-B, M2-P-B, M-P-M-B and state machine models and *in vitro* results after 24 h.

where I is the set of initial conditions, M is the set of measurement types, $v_{i,m}$ is the average of *in vitro* measurement m for the initial condition i , $\sigma_{i,m}$ is the standard deviation of the *in vitro* measurement m for condition i . It is convenient to think of the score as a distance measurement in units of standard deviations between *in vitro* results and model results. Note that the score is actually dimensionless. The genetic algorithm was run for 100 steps at a time. See Appendix A for details on the repopulation of models across generations. To better employ the genetic algorithm as an optimization tool and uncover transition probabilities that represented the experimental data, the best scoring models were used as initial populations of subsequent runs of the algorithm.

2.4. Principle component analysis identifies key transitions

Principle component analysis (PCA) was performed on the entire set of models created during all runs of the genetic algorithm in order to identify key transitions in cell behavior corresponding to the capillary growth observed *in vitro*. Each model's 28 transition probabilities were first reduced to 20. (The probabilities of transitions leaving a state sum to 1, and this restriction means the remaining 8 probabilities can be determined when the 20 are known). We then performed PCA on all models using the reduced set of probabilities. The best scoring models were those that on average were within one standard deviation of *in vitro* results for each measurement (score < 4.2426).

3. Results

We model three cell behaviors by rules based on experimental observations: migration, proliferation and branching. Facilitated by the RAA approach, we then place these individual cell behaviors in context of an organizing structure by the use of a constant-action model, which applies these behaviors in a pre-determined sequence per time-step. To reproduce *in vitro* data more closely than the constant-action model allowed, we next developed state machine models to represent cell behavior, in which the cells do not switch states in a constant sequence but with specified probabilities. These probabilities are derived from our *in vitro* vessel level data with the help of genetic algorithm. Finally, to cluster good state machine models and to find the optimal cell behavior patterns as a function of BDNF and VEGF stimuli, we performed PCA analysis.

The three constant-action models were simulated using six initial growth factor combinations. Fig. 6 shows example capillary growth from the models and the *in vitro* spheroid assay for the same conditions after 24 h with the addition of VEGF and/or BDNF. Quantitative results are presented in Fig. 7 for total vessel length and branch counts for 20 simulations of each model and 10–12 *in vitro* spheroids per condition. The three constant-action models yielded more overall vessel length and branching than the *in vitro* angiogenesis assays under all conditions. We also computed p -values for Welch's t -test comparisons of model results and *in vitro* measurements for total vessel length and branch count. For each model and measurement, the null hypothesis is that the model's mean and the *in vitro* mean are equal. Using this

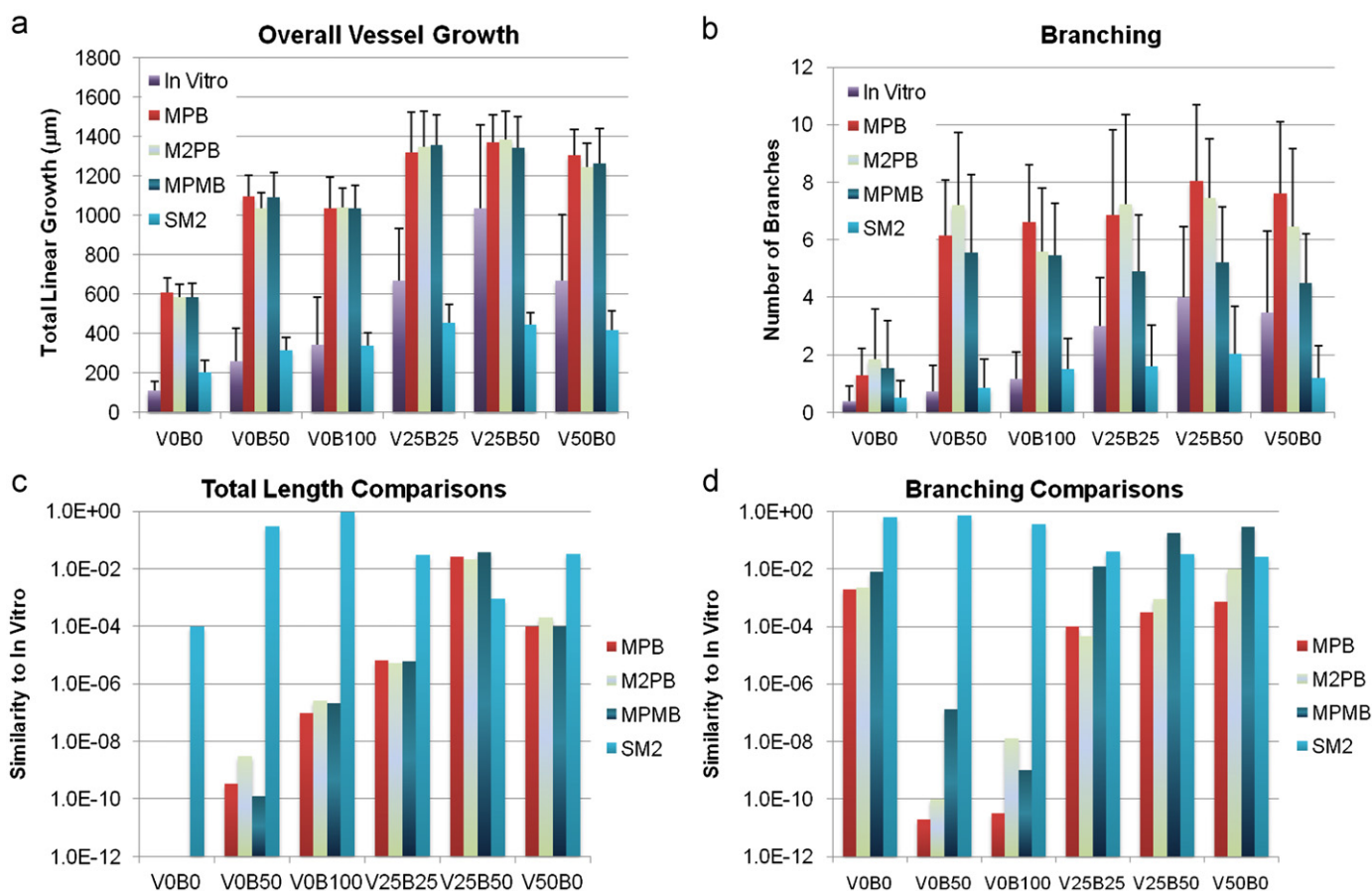


Fig. 7. Quantitative results for angiogenic measurements after 24 h for three constant-action models (M–P–B, M2–P–B, M–P–M–B), the state machine and *in vitro* assays. (a) Overall vessel growth. (b) Branching. Comparison of *in vitro* and model measurements for: (c) total vessel growth, and (d) branching. The y-axis displays the probability of the model output having equivalent means to the experimental measurements. The absence of bars indicates values between 0 and the minimum scale value. Conditions refer to the concentration of VEGF and BDNF in ng/ml; V=VEGF, B=BDNF.

metric, higher p -values indicate a greater probability of model results matching *in vitro* data (Fig. 7c and d).

Figs. 6 and 7 show that the M–P–B and M2–P–B models produce similar linear sprout growth across the combinations of growth factors tested. In contrast, Supplementary Fig. C.3a shows the difference in predicted migration distance (without regard to stalk cell elongation) between the two rules. The Boyden chamber migration rule yields more motile tip cells, but in its implementation, there is negligible long term difference compared to the scratch assay (Supplementary Fig. C.3b). This is because the initial dimensions of the first sprout cells allow them to elongate enough for the difference in migration distances to be clearly evident, but the cell volume increases at each time-step are so low that after the third time-step, the limits on cell elongation severely cap migration distance and effectively hide the difference between the two migration rules.

3.1. Cells as state machines capture cell behavior patterns

However ubiquitous the use of 2D migration and proliferation assays as angiogenesis screens, the assays rarely predict 3D *in vitro* results, let alone *in vivo* or human trials (Goodwin, 2007; Phung and Dass, 2006; Staton et al., 2009). One reason for the discrepancy is that the 2D environment provides different mechanical stimuli and growth factor distribution compared to a 3D assay (Griffith and Swartz, 2006; Lee et al., 2011). Another reason is the cellular events do not exist in isolation like the monolayer assays assume (Zervantonakis et al., 2011). In fact, migration of one cell affects whether an adjacent cell will proliferate or migrate (Yung et al., 2009). The migratory state of a cell also affects whether the cell itself will continue to migrate or decide to proliferate over the next several hours. Ultimately, synergy or inhibition between cell events leads to complex behavior that migration and proliferation assays do not capture. Moreover, existing computational models also do not model this interaction. In order to study synergy and inhibition between behaviors, we augmented our agent-based model with a *state machine* representation of cell activities.

23,130 state machines were created by the genetic algorithm. Models were scored according to the Euclidean distance, as measured in standard deviations, between their simulation results and *in vitro* measurements. Scores assigned to models during actual runs of the algorithm ranged from 3.13 to 607. A model whose performance was one standard deviation away from each of the 18 average *in vitro* measurements received a score of $\sqrt{18} \approx 4.2426$. Accordingly, we defined a *good* state machine as one that received a score of less than 4.2426. The genetic algorithm found 5159 (22%) good models. Both quantitative and qualitative results of the state machine more closely matched *in vitro* data than the constant-action models (Figs. 6 and 7).

The genetic algorithm played an important part in finding state machine transition probabilities. Both the best and worst scoring models of a population improved over generations (Supplementary Fig. C.4a and b), demonstrating the algorithm creates models better than those created at random.

In order to evaluate how properties of the good state machine models related to all other models considered, and whether there were trends of biological significance, principle component analysis was performed on all models. Table 5 shows the loading vectors of the first three principle components. The first, second, and third principle components accounted for 22%, 18% and 14% of the model variation. Much of the variance in models along the first principle component is due to differences in just four key transition probabilities: tip cell idle to migration; tip cell branching to migration; tip cell branching to branching; and stalk cell

Table 5

Loading vectors of the first three principle components computed from all models generated by the genetic algorithm.

Transition	PC1	PC2	PC3
Tip idle → migration	0.46240	0.19970	-0.00180
Tip idle → proliferation	0.05130	-0.01800	-0.00330
Tip idle → branching	0.15880	-0.22790	-0.29140
Tip migration → migration	-0.06460	-0.39530	0.34690
Tip migration → proliferation	0.06170	0.02170	-0.19110
Tip migration → branching	-0.13730	0.19920	-0.26900
Tip proliferation → migration	-0.01460	0.15400	-0.01080
Tip proliferation → proliferation	0.02070	0.15450	-0.04030
Tip proliferation → branching	-0.03080	-0.33240	0.15870
Tip branching → migration	0.33670	-0.09970	0.32120
Tip branching → proliferation	0.08750	0.05580	-0.13870
Tip branching → branching	-0.38230	0.08900	-0.44150
Stalk idle → proliferation	0.08490	0.00530	-0.11680
Stalk idle → branching	-0.00920	-0.47270	-0.07220
Stalk elongation → proliferation	-0.17220	0.10420	0.17600
Stalk elongation → branching	0.13050	-0.03920	-0.31090
Stalk proliferation → proliferation	0.10880	0.15100	0.02430
Stalk proliferation → branching	-0.61910	0.00990	0.26890
Stalk branching → proliferation	0.11400	0.14880	0.11500
Stalk branching → branching	0.02450	-0.50140	-0.33010

proliferation to branching. Fig. 8a shows that the good models form three clusters when plotted along the first three principle components. Average cell behavior transition probabilities for these models are given in Table 6. Notably, they reveal a tendency for tip cells, once idle, to remain idle, and for a stalk cell's idle state to inhibit proliferation in its next time-step. In the time-step after elongation, a stalk cell is most likely to proliferate. Tables 7 and 8 support these observations and give the expected amount of time that the average good state machine would spend in each state and the expected frequency of each transition. Time series images and a video showing the predicted behavior transitions over 2 h for control conditions and stimulated 25 ng/ml VEGF and 50 ng/ml of BDNF of the lowest (best) scoring state machine model shows the cell states by color (Fig. 8b, Supplementary Videos 1 and 2).

As a test of the state machine model's predictive ability, our best scoring state machine model was simulated in 25 ng/ml BDNF, a new condition for which we also had *in vitro* data, for both 24 and 48 h. (All model scoring by the genetic algorithm was for 24 h). Overall vessel length is compared in Fig. 9a, and b provides a visual comparison of simulated and *in vitro* sprouts. The average overall vessel length of the 24 h simulation is near the *in vitro* vessel length and falls between the model results at 0 ng/ml BDNF and 50 ng/ml BDNF (cf. Fig. 7a). State machine overall vessel length measurements were statistically indistinguishable from *in vitro* results at 24 h (p -values for the Welch's t -test were 0.420 for the 24 h simulations and 0.037 for the 48 h simulations).

4. Discussion

Our computational strategy to characterize the sequence and magnitude of cell activities, allows us to quantify how cell behaviors inhibit or augment each other as a function of hypoxic-response associated growth factors. Thus far, the established research literature has studied these behaviors as if they were independent of each other (Supplementary Table D.1). Our results, in contrast, demonstrate how cell migration, proliferation, and branching as functions of local VEGF and BDNF levels can combine synergistically to form new capillary networks from a three-dimensional spheroid of endothelial cells.

Additionally, our results show that a Rules-as-Agents approach to agent-based modeling facilitates the creation and testing of

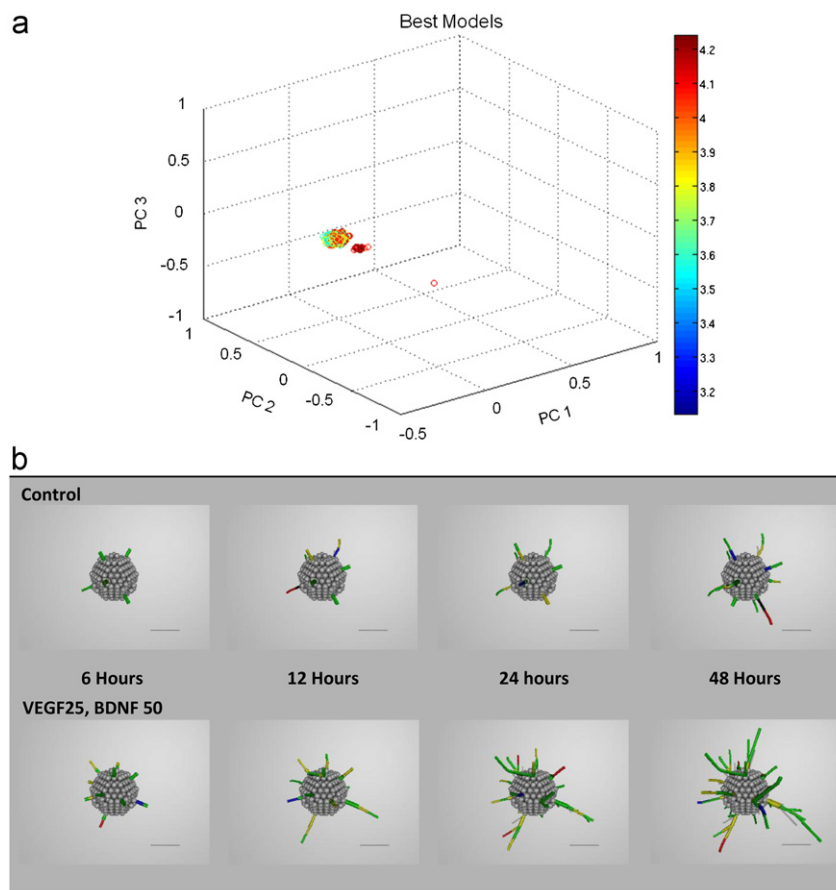


Fig. 8. Best scoring state machines. (a) Best scoring models plotted along the first three principle components. The color bar indicates model score. (b) Examples of the best scoring state machine model sprout growth for: Top: Control. Bottom: 25 ng/ml VEGF, 50 ng/ml BDNF. Cell states are color coded at their respective time-steps: Green=Idle, Blue=Proliferation, Yellow=Branching, Red=Migration, Black=Elongation. Bar=100 μm .

Table 6

Average transition probabilities of the best (score < 4.2426) models found by the genetic algorithm.

Transition	Probability	S.D.
Tip idle→idle	0.818745	0.033507
Tip idle→migration	0.025983	0.010054
Tip idle→proliferation	0.013297	0.001359
Tip idle→branching	0.141976	0.025175
Tip migration→idle	0.293016	0.030733
Tip migration→migration	0.425197	0.033157
Tip migration→proliferation	0.028761	0.002917
Tip migration→branching	0.253026	0.014455
Tip proliferation→idle	0.489085	0.031735
Tip proliferation→migration	0.196429	0.023749
Tip proliferation→proliferation	0.048701	0.015728
Tip proliferation→branching	0.265784	0.015652
Tip branching→idle	0.364617	0.030514
Tip branching→migration	0.139266	0.016486
Tip branching→proliferation	0.068441	0.005337
Tip branching→branching	0.427676	0.026444
Stalk idle→idle	0.587476	0.030834
Stalk idle→proliferation	0.007230	0.001409
Stalk idle→branching	0.405294	0.030370
Stalk elongation→idle	0.351537	0.018693
Stalk elongation→proliferation	0.405778	0.021580
Stalk elongation→branching	0.242685	0.015418
Stalk proliferation→idle	0.210248	0.025398
Stalk proliferation→proliferation	0.089944	0.011623
Stalk proliferation→branching	0.699808	0.034211
Stalk branching→idle	0.515672	0.022490
Stalk branching→proliferation	0.086557	0.010404
Stalk branching→branching	0.397770	0.020385

Table 7

Average expected applications of each behavior rule by cell type over 24 time-steps. These estimates were computed from the state machine specified in Table 6.

	Tip (%)	Stalk A (%)	Stalk B (%)
Idle	68.87	49.60	56.29
Migr./Elong.	8.24	8.24	0.00
Prolif.	2.55	6.41	4.02
Branching	20.33	35.74	39.69
Stalk A—adjacent to tip cell.			
Stalk B—not adjacent to tip cell			

biological hypotheses via computer. It provides a framework to rapidly test different rules and rule organizations for governing cell (or agent) behavior. The separation of rules from the agents that they control and their promotion to the status of agents allows the power of agent-based modeling to apply to the development of rule structure—an entirely novel approach. This technique assists in both the evolution and also the sharing of agent-based models. In previous agent-based models of angiogenesis, the rules that govern agent behavior are part of the agents themselves rather than independent agents. On the other hand, the use of the RAA approach along with Java's packages and dynamic linking feature permit "plug and play" rule modules that can be selected and exchanged at program run-time. This ability speeds the testing of models and also gives the model implementer greater flexibility in creating programs. As such, the RAA approach provides a

Table 8
Average expected usage of individual state machine transitions over 24 time-steps. These estimates were computed from the state machine specified in Table 6.

	Transition	Expected usage (%)	
Tip cell	Idle → idle	56.49	
	Idle → migration	1.79	
	Idle → proliferation	0.92	
	Idle → branching	9.79	
	Migration → idle	2.40	
	Migration → migration	3.49	
	Migration → proliferation	0.24	
	Migration → branching	2.07	
	Proliferation → idle	1.24	
	Proliferation → migration	0.50	
	Proliferation → proliferation	0.12	
	Proliferation → branching	0.68	
	Branching → idle	7.39	
	Branching → migration	2.82	
Branching → proliferation	1.39		
Branching → branching	8.67		
Stalk cell Adjacent to tip	Idle → idle	29.22	
	Idle → proliferation	0.36	
	Idle → branching	20.16	
	Elongation → idle	2.88	
	Elongation → proliferation	3.33	
	Elongation → branching	1.99	
	Proliferation → idle	1.34	
	Proliferation → proliferation	0.57	
	Proliferation → branching	4.46	
	Branching → idle	18.40	
	Branching → proliferation	3.09	
	Branching → branching	14.19	
	Not adjacent tip	Idle → idle	33.13
		Idle → proliferation	0.41
Idle → branching		22.85	
Elongation → idle		0.00	
Elongation → proliferation		0.00	
Elongation → branching		0.00	
Proliferation → idle		0.84	
Proliferation → proliferation		0.36	
Proliferation → branching		2.80	
Branching → idle		20.42	
Branching → proliferation	3.43		
Branching → branching	15.75		

framework in which new cell behavior rules can be added and rule interaction changed with minimal programming. In this paper, we showed the utility of the RAA approach in testing out the effects of different hypothesized migration behaviors and sequences on angiogenesis (Figs. 6 and 7).

Notably, the introduction of a distinct frequency component to individual behaviors via the state machine paradigm allowed us to create a predictive model that produced results that were on the whole better matched to the *in vitro* results, than when we considered the magnitude (and/or direction) of behaviors alone (Figs. 6 and 7). This was done with minimal changes to the individual rule agents, allowing them to maintain fidelity to the previous research from which the rules were originally derived. The relative frequency of cell behaviors as represented by transition probabilities gives a new way to characterize our models as illustrated by the use of PCA to find clusters of good models (Fig. 8a). In general, state machines allow a degree of flexibility in scaling a model over a range of time-steps that constant-action models do not allow. At very small time scales, a constant-action model would implausibly have a cell migrate, proliferate and branch at almost the same time. For large time scales, a state machine model could be augmented to allow transitions representing a combination of actions to occur during a time-step.

We also developed a way to rank competing hypotheses for cell behaviors. Qualitatively, many angiogenesis models produce results that resemble vessel growth, whether the modeling involves

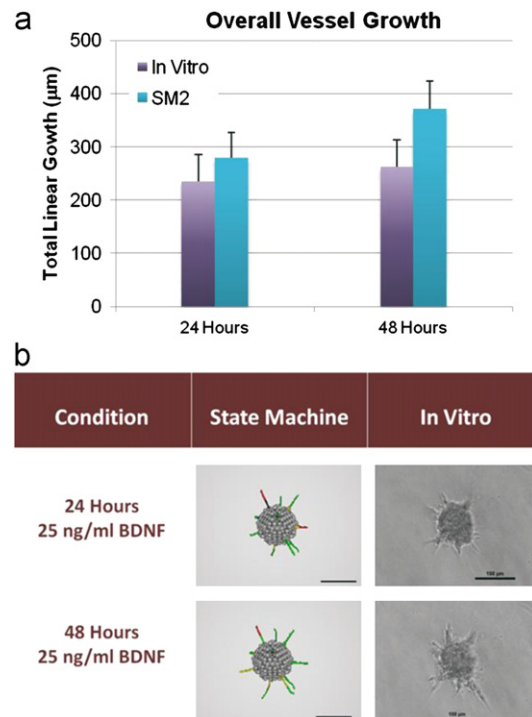


Fig. 9. Model predictions for new cases. (a) Quantitative comparison of *in vitro* overall growth vs. state machine results for criteria (25 ng/ml BDNF and 48 h) not used by the genetic algorithm for state machine selection. (b) Sprout images comparing state machine performance and *in vitro* observations under the novel conditions. Cell states are color coded at the last time-step: Green=Idle, Blue=Proliferation, Yellow=Branching, Red=Migration, Black=Elongation. Bar=100 µm. (For interpretation of the references to color in this figure legend, the reader is referred to the web version of this article.)

differential equations (Chaplain and Anderson, 1996), cellular automata or agents (Bailey et al., 2009; Peirce et al., 2004), or algebraic assumptions (Ji et al., 2006); whether it is 2D or 3D (Qutub et al., 2009a), and whether it employs a Cellular Potts energy minimization assumption (Bauer et al., 2007) or not (Qutub et al., 2009a, 2009b). In select studies, some model output is compared quantitatively with experiments (Bentley et al., 2009; Jakobsson et al., 2010; Peirce et al., 2004; Serini et al., 2003; Thorne et al., 2007). However, there have been no systematic studies exploring the performance of competing angiogenesis models. Here, we quantified the criteria for 'goodness' and ranked competing models. We proposed a strategy where a genetic algorithm runs and scores thousands of agent-based models to choose the sets of cell behavior transitions that correspond best to the observed growth and branching from our experimental assays. This approach is a step towards reverse engineering angiogenesis in terms of individual known cell behaviors. Typically, based on model output, parameters are adjusted in order to align the output with experimental observation. However, we started with no *a priori* theory on cell behavior interactions and used *in vitro* measurements to guide construction of a state machine that controls cell actions to replicate capillary structure.

The key outcome of this analysis is our ability to show distinct patterns in cell behaviors that could give rise to unique capillary phenotypes in the presence of the growth factors VEGF and BDNF (Fig. 8b and Supplementary Videos 1 and 2). The transition probabilities of our state machine directly predict the likelihood of an endothelial cell performing an action based on its last activity. It is of interest to note that in the best scoring models, in the time-step after elongation, a stalk cell is most likely to proliferate. This works to the advantage of tip cell migration. An elongated stalk cell is limited in the amount it can be further elongated, and hence limits subsequent tip cell migration distance, unless the stalk cell

proliferates between elongation phases. In addition, our state machine model was able to transcend the set of *in vitro* measurements used by the genetic algorithm and showed an ability to predict growth for novel situations (Fig. 9). The state machine model and its key transition probabilities (Table 6) predict several interesting cell behavior trends which differ from the constant-action models. Tip cells spend about 82% of their time making transitions involving only the idle and branching states (Tables 7 and 8). Since the probability of branch formation is very low (5–10% per the branching rule and Section 2.2.6), tip cells often remain inactive. In this model, inactivity represents any cell behavior other than migration, proliferation, or branching. Hence, an inactive cell can be performing other activities vital to its own existence or filling an unspecified (not modeled) role in the growth of a sprout. On the occasion that a tip cell migrates, it usually returns to the idle/branching state or migrates again. Although an immediate, second migration behavior yields little movement (Supplementary Fig. C.3b), it does serve to stimulate proliferation in the adjacent stalk cell about 40% of the time. Finally, proliferation is done rarely by tip cells, less than once every 24 h of simulated growth. The dominance of stalk cell proliferation over tip cell proliferation confirms other research on tip cell proliferation (Gerhardt et al., 2003; Hellstrom et al., 2007). Since a single set of transition probabilities was selected by the genetic algorithm to apply to all combinations of growth factors, the transitions in tip cell behavior described here hold regardless of VEGF and BDNF levels. Instead, growth factors manifest themselves as changes in migration distance, proliferation volume, and branching probability. For example an increase in the local concentration of VEGF will result in more proliferation for a cell, but not in more frequent proliferation.

Similarly, stalk cells also spend much of their time in the idle and branching states. Although proliferation is relatively rare for a stalk cell, if any stalk cell does proliferate, it can result in its sprout tip moving (provided that there are no branches between the proliferating cell and the sprout tip) as described in Section 2.2.5. Thus stalk cells collectively act to push the sprout tip forward.

In total, these results lend support to pro-angiogenic therapeutic approaches that target both proliferating stalk cells and activated cells in an “idle” state to help control vasculature phenotypes, through the use of combinatorial BDNF and VEGF stimulation. Despite low rates of proliferation, the contribution of endothelial cell proliferation to the vascular phenotype is biologically significant through its influence on elongation, and statistically, it is a dominant factor in determining overall vessel length and branching (Tables 5 and 6). Results also support that BDNF and VEGF levels contribute to the frequency of cell branching behaviors, and hence modulation of BDNF and VEGF signaling could potentially be used to as a means to regulate capillary network branching. In terms of the interactions between VEGF and BDNF and their influence of vessel morphology, the model and assays support an additive role of the two growth factors in their contribution to vessel length (Fig. 7a), which is consistent in endothelial cells with a proposed feed-forward loop between BDNF–HIF1 α –VEGF, previously shown in neuroblastoma cells (Nakamura et al., 2006). Targeting both of these compounds, rather than one, would then be expected to yield the greatest control of endothelial cell proliferation and branching frequency, and hence overall growth potential. Notably, the vessel branching rate appears significantly more stochastic *in vitro* and in our state machines than overall vessel length, and less influenced by levels of the two growth factors (Fig. 7b).

Along with the benefits of the model, limitations of the current implementation should also be noted. VEGF and BDNF concentrations were assumed uniform in space and constant in time. This does not reflect the behavior of these growth factors in *in vivo* circumstances and simplifies the *in vitro* conditions. Only three basic cell behaviors were modeled, whereas other behaviors such as anastomosis and apoptosis have also been identified as playing a part in angiogenesis.

The current study has also been limited to the first 24 h of sprout growth. The RAA framework of our modeling paradigm allows for these and other considerations to be readily revised as our experimental knowledge expands.

Since our starting point relies on our interpretation of *in vitro* observations of cell actions as distinct behaviors we call “migration”, “proliferation”, and “branching”, our model is subject to refinement as we learn more about endothelial cell behavior. We are open to the possibility that an attempt to map, say, migration to subcellular processes may reveal a constellation of microstates that combine to effect migration and other behaviors. Still, we are confident that our approach would be applicable and could help to form a descriptive bridge between the original cell behaviors that we have observed and cellular processes that may be better described by other modeling techniques.

In sum, the results presented here are a step towards understanding and quantifying patterns of cell behaviors as a function of the local microenvironment. We have predicted the patterns of endothelial cell decisions (“behavior signatures”) which gave rise to unique capillary phenotypes as a function of VEGF and BDNF, shown the utility of the state-machine paradigm in capturing cell behaviors, and uncovered key behavior transitions that can now be tested experimentally. Recently proposed regenerative therapies aimed at stroke and neurodegenerative diseases share a common feature: they are multi-modal and affect multiple cell behaviors (Freeman and Barone, 2005; Harten et al., 2010; Wu et al., 2010; Zhang and Chopp, 2009). By applying our modeling to new growth factor conditions or targeting cell behaviors in the state machine, the presented approach can be used to help test and guide the development of vascular regenerative therapies.

5. Conclusions

We presented an integrated experimental–computational strategy to characterize cell behavior patterns from capillary structures. The state machine paradigm allowed us to explore the difference between the frequency and intensity of cell behaviors. A key benefit of this approach is to understand how the synergy or inhibition between cell events leads to complex behavior that migration and proliferation assays do not capture. Using our technological advances, we predicted the patterns of endothelial cell decisions which gave rise to unique capillary phenotypes as a function of combinations of VEGF and BDNF levels. These results offer the ability to understand – and ultimately help to control – human cell behavior of the microvasculature. Our RAA framework allows rapid hypothesis testing, useable in research across labs and fields. Overall, the integrated state machine-genetic algorithm introduced here can be broadly applied to study patterns in cell behavior, which can in turn be linked to molecular signaling. Insight from this work will allow us to help guide vessel regeneration strategies for neurovascular diseases.

Acknowledgments

This work was supported in part by a National Academies Keck Future Initiatives grant, a Hamill Innovation Award and National Science Foundation CAREER Award 1150645.

Appendix A. Supporting information

Supplementary data associated with this article can be found in the online version at <http://dx.doi.org/10.1016/j.jtbi.2012.11.030>.

References

Alberts, B., Johnson, A., Lewis, J., Raff, M., Roberts, K., Walter, P., 2002. Molecular Biology of the Cell, fourth ed. Garland Science.

- Arai, K., Jin, G., Navaratna, D., Lo, E.H., 2009. Brain angiogenesis in developmental and pathological processes: neurovascular injury and angiogenic recovery after stroke. *FEBS J.* 276, 4644–4652.
- Artel, A., Mehdizadeh, H., Chiu, Y.-C., Brey, E.M., Cinar, A., 2011. An agent-based model for the investigation of neovascularization within porous scaffolds. *Tissue Eng. Part A* 17, 2133–2141.
- Bailey, A.M., Thorne, B.C., Peirce, S.M., 2007. Multi-cell agent-based simulation of the microvasculature to study the dynamics of circulating inflammatory cell trafficking. *Ann. Biomed. Eng.* 35, 916–936.
- Bailey, A.M., Lawrence, M.B., Shang, H., Katz, A.J., Peirce, S.M., 2009. Agent-based model of therapeutic adipose-derived stromal cell trafficking during ischemia predicts ability to roll on P-selectin. *PLoS Comput. Biol.* 5, e1000294.
- Bauer, A.L., Jackson, T.L., Jiang, Y., 2007. A cell-based model exhibiting branching and anastomosis during tumor-induced angiogenesis. *Biophys. J.* 92, 3105–3121.
- Beck, H., Plate, K.H., 2009. Angiogenesis after cerebral ischemia. *Acta Neuropathol.* 117, 481–496.
- Bentley, K., Gerhardt, H., Bates, P.A., 2008. Agent-based simulation of notch-mediated tip cell selection in angiogenic sprout initialisation. *J. Theor. Biol.* 250, 25–36.
- Bentley, K., Mariggi, G., Gerhardt, H., Bates, P.A., 2009. Tipping the balance: robustness of tip cell selection, migration and fusion in angiogenesis. *PLoS Comput. Biol.* 5, e1000549.
- Bonabeau, E., 2002. Agent-based modeling: methods and techniques for simulating human systems. *Proc. Nat. Acad. Sci. U.S.A.* 99 (Suppl 3), 7280–7287.
- Carmeliet, P., Tessier-Lavigne, M., 2005. Common mechanisms of nerve and blood vessel wiring. *Nature* 436, 193–200.
- Chang, H., Wang, B.-W., Kuan, P., Shyu, K.-G., 2003. Cyclical mechanical stretch enhances angiotensin-2 and Tie2 receptor expression in cultured human umbilical vein endothelial cells. *Clin. Sci.* 104, 421–428.
- Chaplain, M.A., Anderson, A.R., 1996. Mathematical modelling, simulation and prediction of tumour-induced angiogenesis. *Invasion Metastasis* 16, 222–234.
- Chen, K., Henry, R.A., Hughes, S.M., Connor, B., 2007. Creating a neurogenic environment: the role of BDNF and FGF2. *Mol. Cell. Neurosci.* 36, 108–120.
- Conway, J., Sloane, N., 1999. *Sphere Packings, Lattices and Groups*. Springer, New York.
- Croll, S.D., Wiegand, S.J., 2001. Vascular growth factors in cerebral ischemia. *Mol. Neurobiol.* 23, 121–135.
- Das, A., Lauffenburger, D., Asada, H., Kamm, R.D., 2010. A hybrid continuum-discrete modelling approach to predict and control angiogenesis: analysis of combinatorial growth factor and matrix effects on vessel-sprouting morphology. *Philos. Trans. A Math. Phys. Eng. Sci.* 368, 2937–2960.
- Dimmeler, S., Dernbach, E., Zeiher, A.M., 2000. Phosphorylation of the endothelial nitric oxide synthase at Ser-1177 is required for VEGF-induced endothelial cell migration. *FEBS Lett.* 477, 258–262.
- Engelberg, J.A., Datta, A., Mostov, K.E., Hunt, C.A., 2011. MDCK cystogenesis driven by cell stabilization within computational analogues. *PLoS Comput. Biol.* 7, e1002030.
- Freeman, R.S., Barone, M.C., 2005. Targeting hypoxia-inducible factor (HIF) as a therapeutic strategy for CNS disorders. *Curr. Drug Targets CNS Neurol. Disord.* 4, 85–92.
- Gerhardt, H., Golding, M., Fruttiger, M., Ruhrberg, C., Lundkvist, A., Abramsson, A., Jeltsch, M., Mitchell, C., Alitalo, K., Shimada, D., Betsholtz, C., 2003. VEGF guides angiogenic sprouting utilizing endothelial tip cell filopodia. *J. Cell Biol.* 161, 1163–1177, <http://dx.doi.org/10.1083/jcb.200302047>.
- Goodwin, A.M., 2007. *In vitro* assays of angiogenesis for assessment of angiogenic and anti-angiogenic agents. *Microvasc. Res.* 74, 172–183.
- Griffith, L.G., Swartz, M.A., 2006. Capturing complex 3D tissue physiology *in vitro*. *Nat. Rev. Mol. Cell Biol.* 7, 211–224.
- Grinstead, C.M., Snell, J.L., 1997. *Introduction to Probability*. American Mathematical Society.
- Harms, B.D., Bassi, G.M., Horwitz, A.R., Lauffenburger, D.A., 2005. Directional persistence of EGF-induced cell migration is associated with stabilization of lamellipodial protrusions. *Biophys. J.* 88, 1479–1488.
- Harten, S.K., Ashcroft, M., Maxwell, P.H., 2010. Prolyl hydroxylase domain inhibitors: a route to HIF activation and neuroprotection. *Antioxid Redox Signal* 12, 459–480.
- Hellstrom, M., Phng, L.-K., Hofmann, J.J., Wallgard, E., Coultas, L., Lindblom, P., Alva, J., Nilsson, A.-K., Karlsson, L., Gaiano, N., Yoon, K., Rossant, J., Iruela-Arispe, M.L., Kalen, M., Gerhardt, H., Betsholtz, C., 2007. Dll4 signalling through Notch1 regulates formation of tip cells during angiogenesis. *Nature* 445, 776–780.
- Jakobsson, L., Franco, C.A., Bentley, K., Collins, R.T., Ponsioen, B., Aspö, I.M., Rosewell, I., Busse, M., Thurston, G., Medvinsky, A., Schulte-Merker, S., Gerhardt, H., 2010. Endothelial cells dynamically compete for the tip cell position during angiogenic sprouting. *Nat. Cell Biol.* 12, 943–953.
- Ji, J.W., Tsoukias, N.M., Goldman, D., Popel, A.S., 2006. A computational model of oxygen transport in skeletal muscle for sprouting and splitting modes of angiogenesis. *J. Theor. Biol.* 241, 94–108.
- Jin, K.L., Mao, X.O., Nagayama, T., Goldsmith, P.C., Greenberg, D.A., 2000. Induction of vascular endothelial growth factor and hypoxia-inducible factor-1 α by global ischemia in rat brain. *Neuroscience* 99, 577–585.
- Korff, T., Augustin, H.G., 1998. Integration of endothelial cells in multicellular spheroids prevents apoptosis and induces differentiation. *J. Cell Biol.* 143, 1341–1352.
- Korff, T., Augustin, H.G., 1999. Tensional forces in fibrillar extracellular matrices control directional capillary sprouting. *J. Cell Sci.* 112, 3249–3258.
- Laib, A.M., Bartol, A., Alajati, A., Korff, T., Weber, H., Augustin, H.G., 2009. Spheroid-based human endothelial cell microvessel formation *in vivo*. *Nat. Protoc.* 4, 1202–1215.
- Lee, H.S., Han, J., Bai, H.J., Kim, K.W., 2009. Brain angiogenesis in developmental and pathological processes: regulation, molecular and cellular communication at the neurovascular interface. *FEBS J.* 276, 4622–4635.
- Lee, K., Silva, E.A., Mooney, D.J., 2011. Growth factor delivery-based tissue engineering: general approaches and a review of recent developments. *J. R. Soc. Interface* 8, 153–170.
- Liu, G., Qutub, A.A., Vempati, P., Mac Gabhann, F., Popel, A.S., 2011. Module-based multiscale simulation of angiogenesis in skeletal muscle. *Theor. Biol. Med. Modell.* 8, 6.
- Maes, P., 1994. Modeling adaptive autonomous agents. *Artif. Life*, 1–37.
- Manoonkitiwongsa, P.S., Schultz, R.L., McCreery, D.B., Whitter, E.F., Lyden, P.D., 2004. Neuroprotection of ischemic brain by vascular endothelial growth factor is critically dependent on proper dosage and may be compromised by angiogenesis. *J. Cereb. Blood Flow Metab.* 24, 693–702.
- Manso, H., Krug, T., Sobral, J., Albergaria, I., Gaspar, G., Ferro, J.M., Oliveira, S.A., Vicente, A.M., 2012. Evidence for epistatic gene interactions between growth factor genes in stroke outcome. *Eur. J. Neurol.*
- McLaughlin, A.P., De Vries, G.W., 2001. Role of PLC γ and Ca(2+) in VEGF- and FGF-induced choroidal endothelial cell proliferation. *Am. J. Physiol. Cell Physiol.* 281, C1448–C1456.
- Merks, R.M., Perryn, E.D., Shirinifard, A., Glazier, J.A., 2008. Contact-inhibited chemotaxis in de novo and sprouting blood-vessel growth. *PLoS Comput. Biol.* 4, e1000163.
- Merks, R.M., Brodsky, S.V., Goligorsky, M.S., Newman, S.A., Glazier, J.A., 2006. Cell elongation is key to *in silico* replication of *in vitro* vasculogenesis and subsequent remodeling. *Dev. Biol.* 289, 44–54.
- Mu, D., Jiang, X., Sheldon, R.A., Fox, C.K., Hamrick, S.E., Vexler, Z.S., Ferriero, D.M., 2003. Regulation of hypoxia-inducible factor 1 α and induction of vascular endothelial growth factor in a rat neonatal stroke model. *Neurobiol. Dis.* 14, 524–534.
- Mukoyama, Y.S., Shin, D., Britsch, S., Taniguchi, M., Anderson, D.J., 2002. Sensory nerves determine the pattern of arterial differentiation and blood vessel branching in the skin. *Cell* 109, 693–705.
- Nakamura, K., Martin, K.C., Jackson, J.K., Beppu, K., Woo, C.-W., Thiele, C.J., 2006. Brain-derived neurotrophic factor activation of TrkB induces vascular endothelial growth factor expression via hypoxia-inducible factor-1 α in neuroblastoma cells. *Cancer Res.* 66, 4249–4255, <http://dx.doi.org/10.1158/0008-5472.can-05-2789>.
- Nakashio, A., Fujita, N., Tsuruo, T., 2002. Topotecan inhibits VEGF- and bFGF-induced vascular endothelial cell migration via downregulation of the PI3K-Akt signaling pathway. *Int. J. Cancer* 98, 36–41.
- Neufeld, A.H., Jumblatt, M.M., Matkin, E.D., Raymond, G.M., 1986. Maintenance of corneal endothelial cell shape by prostaglandin E2: effects of EGF and indomethacin. *Invest. Ophthalmol. Vis. Sci.* 27, 1437–1442.
- Noiri, E., Lee, E., Testa, J., Quigley, J., Colflesh, D., Keese, C.R., Gjaever, I., Goligorsky, M.S., 1998. Podokinesis in endothelial cell migration: role of nitric oxide. *Am. J. Physiol.* 274, C236–C244.
- Peirce, S.M., Van Gieson, E.J., Skalak, T.C., 2004. Multicellular simulation predicts microvascular patterning and *in silico* tissue assembly. *FASEB J.* 18, 731–733.
- Phung, M.W., Dass, C.R., 2006. *In-vitro* and *in-vivo* assays for angiogenesis-modulating drug discovery and development. *J. Pharm. Pharmacol.* 58, 153–160.
- Pichiule, P., Agani, F., Chavez, J.C., Xu, K., LaManna, J.C., 2003. HIF-1 α and VEGF expression after transient global cerebral ischemia. *Adv. Exp. Med. Biol.* 530, 611–617.
- Poche, R.A., Saik, J.E., West, J.L., Dickinson, M.E., 2010. The mouse cornea as a transplantation site for live imaging of engineered tissue constructs. *Cold Spring Harb. Protoc.* 2010, pdb prot5416.
- Qu, R., Li, Y., Gao, Q., Shen, L., Zhang, J., Liu, Z., Chen, X., Chopp, M., 2007. Neurotrophic and growth factor gene expression profiling of mouse bone marrow stromal cells induced by ischemic brain extracts. *Neuropathology* 27, 355–363.
- Qutub, A., Gabhann, F., Karagiannis, E., Vempati, P., Popel, A., 2009a. Multiscale models of angiogenesis. *IEEE Eng. Med. Biol. Mag.* 28, 14–31.
- Qutub, A.A., Popel, A.S., 2009. Elongation, proliferation & migration differentiate endothelial cell phenotypes and determine capillary sprouting. *BMC Syst. Biol.* 3, 13.
- Qutub, A.A., Liu, G., Vempati, P., Popel, A.S., 2009b. Integration of angiogenesis modules at multiple scales: from molecular to tissue. *Pac. Symp. Biocomput.*, 316–327.
- Ratan, R.R., Siddiq, A., Smirnova, N., Karpisheva, K., Haskew-Layton, R., McConoughey, S., Langley, B., Estevez, A., Huerta, P.T., Volpe, B., Roy, S., Sen, C.K., Gazaryan, I., Cho, S., Fink, M., LaManna, J., 2007. Harnessing hypoxic adaptation to prevent, treat, and repair stroke. *J. Mol. Med.* 85, 1331–1338.
- Ropella, G.E., Hunt, C.A., 2010. Cloud computing and validation of expandable *in silico* livers. *BMC Syst. Biol.* 4, 168.
- Rupp, P.A., Czirik, A., Little, C.D., 2004. $\alpha\beta$ 3 integrin-dependent endothelial cell dynamics *in vivo*. *Development* 131, 2887–2897, <http://dx.doi.org/10.1242/dev.01160>.
- Serini, G., Ambrosi, D., Giraudo, E., Gamba, A., Preziosi, L., Bussolino, F., 2003. Modeling the early stages of vascular network assembly. *EMBO J.* 22, 1771–1779.

- Sheikh-Bahaei, S., Hunt, C.A., 2011. Enabling clearance predictions to emerge from *in silico* actions of quasi-autonomous hepatocyte components. *Drug Metab. Dispos.*
- Shi, Q., Zhang, P., Zhang, J., Chen, X., Lu, H., Tian, Y., Parker, T.L., Liu, Y., 2009. Adenovirus-mediated brain-derived neurotrophic factor expression regulated by hypoxia response element protects brain from injury of transient middle cerebral artery occlusion in mice. *Neurosci. Lett.* 465, 220–225, <http://dx.doi.org/10.1016/j.neulet.2009.08.049>.
- Staton, C.A., Reed, M.W., Brown, N.J., 2009. A critical analysis of current *in vitro* and *in vivo* angiogenesis assays. *Int. J. Exp. Pathol.* 90, 195–221.
- Stokes, C.L., Lauffenburger, D.A., Williams, S.K., 1991. Migration of individual microvessel endothelial cells: stochastic model and parameter measurement. *J. Cell Sci.* 99, 419–430.
- Sun, Y., Jin, K., Xie, L., Childs, J., Mao, X.O., Logvinova, A., Greenberg, D.A., 2003. VEGF-induced neuroprotection, neurogenesis, and angiogenesis after focal cerebral ischemia. *J. Clin. Invest.* 111, 1843–1851.
- Thorne, B.C., Bailey, A.M., Peirce, S.M., 2007. Combining experiments with multi-cell agent-based modeling to study biological tissue patterning. *Brief. Bioinform.* 8, 245–257.
- Varma, S., Lal, B.K., Zheng, R., Breslin, J.W., Saito, S., Pappas, P.J., Hobson, W., Durán, I., W. N., 2005. Hyperglycemia alters PI3k and Akt signaling and leads to endothelial cell proliferative dysfunction. *Am. J. Physiol.—Heart Circ. Physiol.* 289, H1744–H1751.
- Wang, B.W., Chang, H., Lin, S., Kuan, P., Shyu, K.G., 2003. Induction of matrix metalloproteinases-14 and -2 by cyclical mechanical stretch is mediated by tumor necrosis factor- α in cultured human umbilical vein endothelial cells. *Cardiovasc. Res.* 59, 460–469.
- Wilson, B.D., Li, M., Park, K.W., Suli, A., Sorensen, L.K., Larriue-Lahargue, F., Urness, L.D., Suh, W., Asai, J., Kock, G.A., Thorne, T., Silver, M., Thomas, K.R., Chien, C.B., Losordo, D.W., Li, D.Y., 2006. Netrins promote developmental and therapeutic angiogenesis. *Science* 313, 640–644.
- Wu, G., Luo, J., Rana, J.S., Laham, R., Sellke, F.W., Li, J., 2006. Involvement of COX-2 in VEGF-induced angiogenesis via P38 and JNK pathways in vascular endothelial cells. *Cardiovasc. Res.* 69, 512–519, <http://dx.doi.org/10.1016/j.cardiores.2005.09.019>.
- Wu, L.-W., Mayo, L.D., Dunbar, J.D., Kessler, K.M., Baerwald, M.R., Jaffe, E.A., Wang, D., Warren, R.S., Donner, D.B., 2000. Utilization of distinct signaling pathways by receptors for vascular endothelial cell growth factor and other mitogens in the induction of endothelial cell proliferation. *J. Biol. Chem.* 275, 5096–5103.
- Wu, W., Chen, X., Hu, C., Li, J., Yu, Z., Cai, W., 2010. Transplantation of neural stem cells expressing hypoxia-inducible factor-1 α (HIF-1 α) improves behavioral recovery in a rat stroke model. *J. Clin. Neurosci.* 17, 92–95, <http://dx.doi.org/10.1016/j.jocn.2009.03.039>.
- Yamaguchi, N., Anand-Apte, B., Lee, M., Sasaki, T., Fukai, N., Shapiro, R., Que, I., Lowik, C., Timpl, R., Olsen, B.R., 1999. Endostatin inhibits VEGF-induced endothelial cell migration and tumor growth independently of zinc binding. *EMBO J.* 18, 4414–4423.
- Yu, P.K., Yu, D., Alder, V.A., Seydel, U., Su, E., Cringle, S.J., 1997. Heterogeneous endothelial cell structure along the porcine retinal microvasculature. *Exp. Eye Res.* 65, 379–389.
- Yung, Y.C., Chae, J., Buehler, M.J., Hunter, C.P., Mooney, D.J., 2009. Cyclic tensile strain triggers a sequence of autocrine and paracrine signaling to regulate angiogenic sprouting in human vascular cells. *Proc. Nat. Acad. Sci. U.S.A.* 106, 15279–15284.
- Zervantonakis, I.K., Kothapalli, C.R., Chung, S., Sudo, R., Kamm, R.D., 2011. Microfluidic devices for studying heterotypic cell–cell interactions and tissue specimen cultures under controlled microenvironments. *Biomicrofluidics* 5, 13406.
- Zhang, Z.G., Chopp, M., 2009. Neurorestorative therapies for stroke: underlying mechanisms and translation to the clinic. *Lancet Neurol.* 8, 491–500.

Appendices

Appendix A. Methodology of the Agent-Based Model Implementation

Appendix B. Quantification of Results

Appendix C. Supplementary Figures

Appendix D. Supplementary Tables

Appendix A. Methodology of the Agent-Based Model Implementation

1. Model Details

1.1 Determination of Cell Proliferation Rates

The rule for a cell's volume increase was determined from *in vitro* experiments. First, a baseline proliferation rate for endothelial cells was calculated from the logistic-shaped portion of the growth curve in previous research on proliferation (Varma et al., 2005). This was approximated by the Verhulst model (Verhulst, 1838) relating population and time:

$$\frac{dN}{dt} = rN \left(1 - \frac{N}{K}\right)$$

where r is the growth rate and K is an asymptotic population maximum. The solution can be expressed as:

$$N(t) = \frac{KN_0}{(K - N_0)e^{-rt} + N_0}$$

where N_0 is the size of the initial population. This curve can be fit to the data by first re-expressing it:

$$\ln\left(\frac{KN_0}{N(t)} - N_0\right) = -rt + \ln(K - N_0)$$

We then let:

$$\alpha = \ln\left(\frac{KN_0}{N(t)} - N_0\right)$$

The linear regression of Supplementary Figure C.1c then gives the baseline endothelial growth rate parameter, g_{baseline} . This calculation of the growth rate is then used in a uniform way that is consistent with constant-action models – that a growth rate for a group can be uniformly applied to individual cells provided that each cell performs its proliferation behavior at each time-step. (Equation 4A) However, in a state machine model, this situation is different because proliferation need not be performed at every time-step. A rate of volume increase for when a cell is actually proliferating is required. Under the assumption that at any moment, n_{active} fraction of a group of cells is actively proliferating, the baseline growth rate is adjusted as per Equation 4B.

Studies have shown a positive correlation between BDNF and endothelial cell proliferation (Lam et al., 2011) and proliferation related metrics such as vessel density (Kermani et al., 2005), vessel length (Kim et al., 2004) and vessel structure count (Hu et al., 2007). However, BDNF is introduced into the biological system of study by many ways, such as by injection into tissue (Hu et al., 2007) and genetically engineering cells to produce BDNF (Kermani et al., 2005; Kim et al., 2004; Lam et al., 2011), that cannot readily be translated into our model. Since all of these correlations are positive compared to control, we decided to include the effect of BDNF on proliferation as a threshold model (see Equation 4A).

1.2 Modeling of Growth Factors

VEGF and BDNF concentrations were modeled as being uniform in space and constant in time. Endothelial cells in the model sense these levels, but do not alter them.

1.3 Cell Junctions

There are only two types of sprout cell junctions: two-cell junctions and three-cell junctions. A two-cell junction is typical along a sprout and is formed from two cells when the rear end of a cell is connected to the front end of the cell behind it. A three-cell junction is formed when a branch is created. A new branch cell has its rear end connected at the same point as the original cell. Thus the rear ends of two cells are connected to the front end of another cell. Since there are no four-cell junctions, a sprout can split into two branches, but not more than two at any particular location.

2. Genetic Algorithm

A genetic algorithm is a biologically inspired search technique that abstractly mimics evolution (Whitley, 1994). An initial generation of a population is created (usually at random) and each member is assigned a fitness score. Members with better scores survive into the next generation where they are used to create new members to replace those that did not survive. This score-cull-regenerate cycle typically repeats until a limit in the number of generations is reached or an acceptable member is found. See Figure 5e. A genetic algorithm is useful when the structure of the set of possible members to be searched is not well understood. It is also appropriate if the search space has local minima. In our model the fitness score was defined by the 18-dimensional distance between the model results and experiments (Equation (*), Section 2.3).

Each successive generation was replenished with new models created by combining two surviving models. To create each new model, two different surviving models were selected at random. For each transition probability in the new model one of the corresponding transition probabilities was selected at random from the two models with probability p that the transition from the higher scoring (worse) model would be chosen. The selected probability was then mutated by scaling it by a randomly selected factor between $1 - m$ and $1 + m$. After these values are computed, they are normalized so that for each state, probabilities of outgoing transitions sum to 1 (see Figure 5f). Both p and m are functions of the generation number and decay towards 0. The intended effect is that models created in later generations are more similar to a parent model than those created in earlier generations.

Performance of the genetic search was measured in terms of the best and worst models at each generation. Supplemental Figure C.4a shows how the score of the best model changed during the first 8

runs of the algorithm. Each time, the search procedure started with a population of models randomly created. The preservation of the top models across generations by our implementation acted as a ratchet that prevented the top model at each generation from having a worse score than that of a previous generation. This raised the question that our method for creating new models to replenish a culled population might be no better than simply creating new models at random. In the case of replenishment by randomly created models, we would expect that the worst model at each generation would usually be a newly created one and its score subject to fluctuations both up and down due to the random way in which it was created. Supplemental Figure C.4b shows that although there were slight fluctuations, the scores of the worst models dropped in a manner similar to that of the best models. Hence each population as a whole was being improved by our method of creating new models in a way that replenishment at random could not.

3. Implementation Notes

3.1 Rules-As-Agents

To rapidly explore and test different ways that rules for behaviors can be combined, we developed a Rules-As-Agents architecture (RAA). Typically in agent-based modeling, the rules that control an agent are considered to be part of the agent itself (Fig. 5a). The RAA separates the rules from their cell agents and promotes them to the status of agents themselves. Migration, proliferation, and branching rules are separate entities from cells. To organize these rules, we created a rules manager. The rules manager is responsible for controlling rule interactions and also serves as a central receiver of behavior requests from cell agents (Supplementary Fig. 5a). A standardized rule-cell interface was defined for rule agents to command cell agents to act.

3.2 Modularity

The simulator was designed with the goal of allowing independent development of modules for basic endothelial cell behavior, angiogenesis rules controlling endothelial cells, growth factor diffusion rules, physical geometry, and a graphical user interface. Along with this goal was the desire to limit the extent to which modules could interfere with each other.

The implementation architecture is given in Supplementary Figure C.5a. Simulations are controlled by the model environment module which serves as the simulation engine. It starts/initializes all other modules, serves parameters, steps the agents during the simulation, and collects statistics.

3.3 Simulations

The models were implemented in the Java programming language (version 1.6) using the MASON simulation toolkit (<http://cs.gmu.edu/~eclab/projects/mason/>). Simulations were performed on a Lenovo TS200 server with 24 GB of main memory running Red Hat Linux. Simulation output was rendered by the POV-Ray ray tracing tool (version 3.6.1). Principle component analysis was done in MATLAB (version 7.10.0).

Appendix B. Quantification of Results

Measurements

Measurements of simulation results were taken directly from the implementation's data structures. In order to be consistent with *in vitro* measurements, simulation measurements were taken after the three-dimensional sprout data was projected onto the $Z=0$ plane. The sphere into which the initial cells were packed was also projected onto the same plane. Any sprout growth or branches within this circular projection were not measured. Sprout lengths were calculated by summing the lengths of cylinder axes. Branches were identified by locating the rearmost point of the branch, where two cylinder axes intersect. Thus if a branch started within the circular projection of the initial cell cluster, the growth was not considered as a branch, but the part or parts of it outside of the sphere projection were included in the total growth measurement.

Appendix C. Supplementary Figures

Supplementary Figure C.1. Model parameter derivation. Graphs depicting how the rules were obtained for migration using the scratch assay (a), migration using the Boyden chamber assay (b), baseline proliferation (c), and proliferation as a function of VEGF (d).

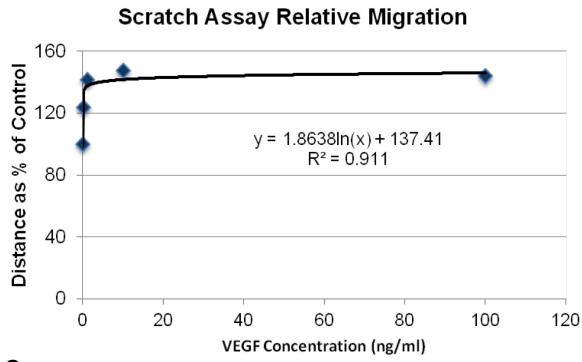
Supplementary Figure C.2. An example of state machines for tip cells and stalk cells. Each transition is labeled with a probability. The dashed arrow represents a tip cell's migration state forcing its adjacent stalk cell to its elongation state.

Supplementary Figure C.3. Migration rule performance. (a) Comparison of migration rules derived from the Boyden chamber assay and the scratch assay without regard to the effects of stalk cell elongation. Distance is per one hour time-step. (b) Actual migration distances over the course of a simulation at VEGF 50ng/ml. Each time-step is one hour. The ability of a stalk cell to increase its volume and then elongate limits tip cell migration distance.

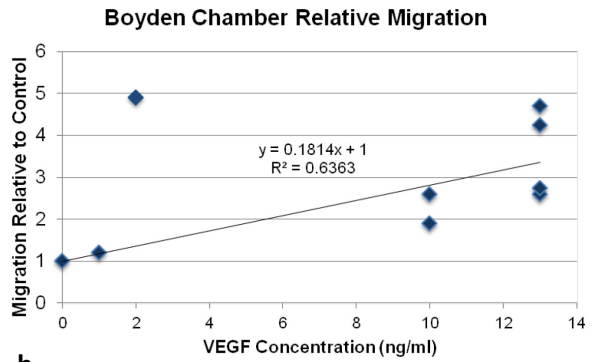
Supplementary Figure C.4. Genetic algorithm performance. Scores of the best (a) and worst (b) models at each generation for 8 runs of the genetic algorithm. First generation worst model scores are not displayed and ranged from 63.5 to 607.4.

Supplementary Figure C.5. Model implementation. (a) Model Architecture. The rule-oriented portion of the model is at left. An arrow from one module to a second indicates method invocation of the second by the first. (b) Flow diagram showing behavior of endothelial cells in a time-step. The order of cell events is a model parameter.

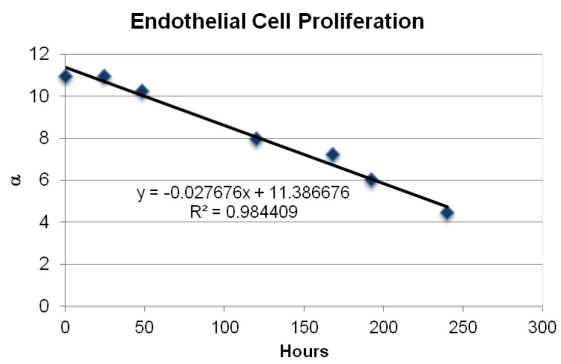
Supplementary Figure C.1.



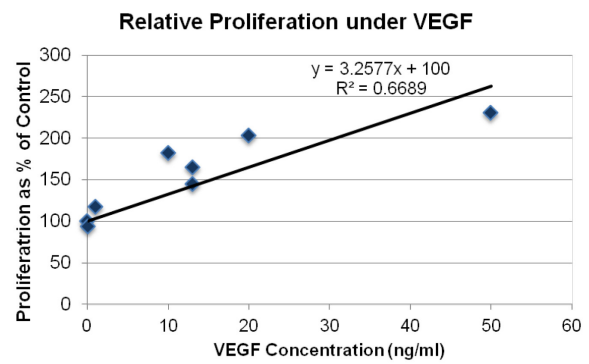
a



b

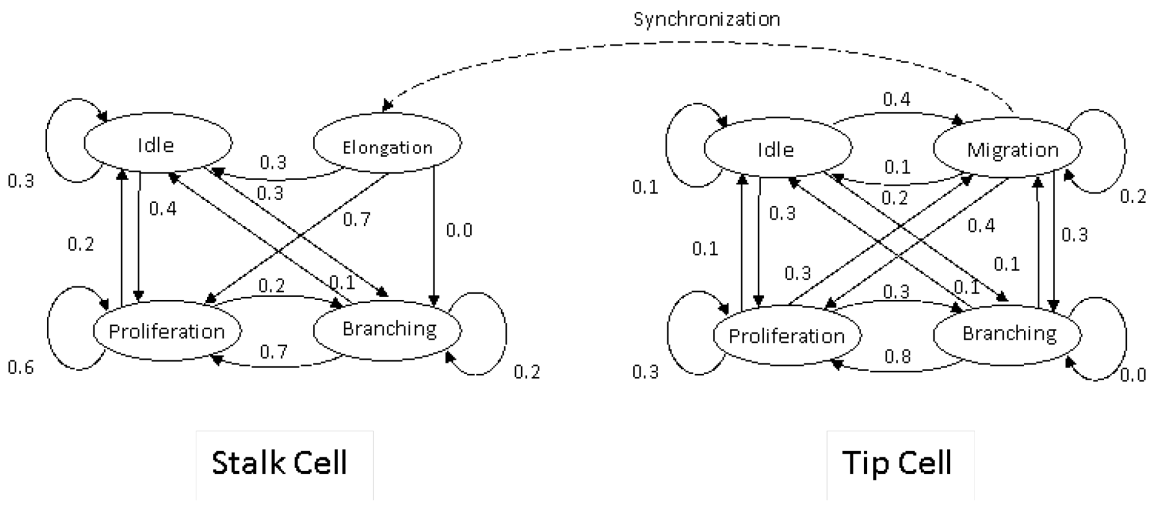


c



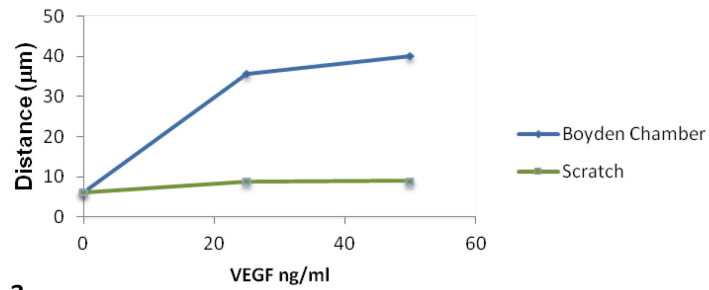
d

Supplementary Figure C.2.



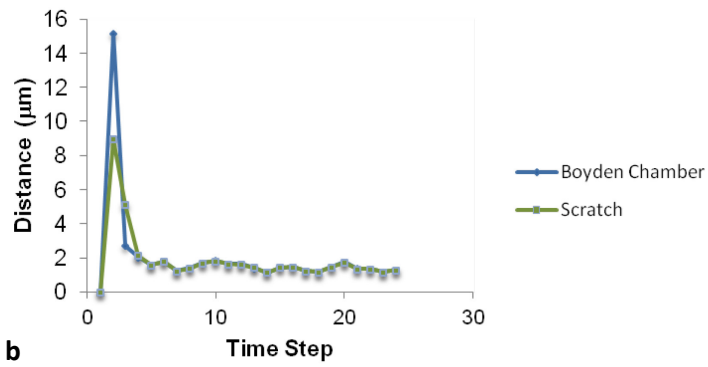
Supplementary Figure C.3.

Attempted Migration Distance



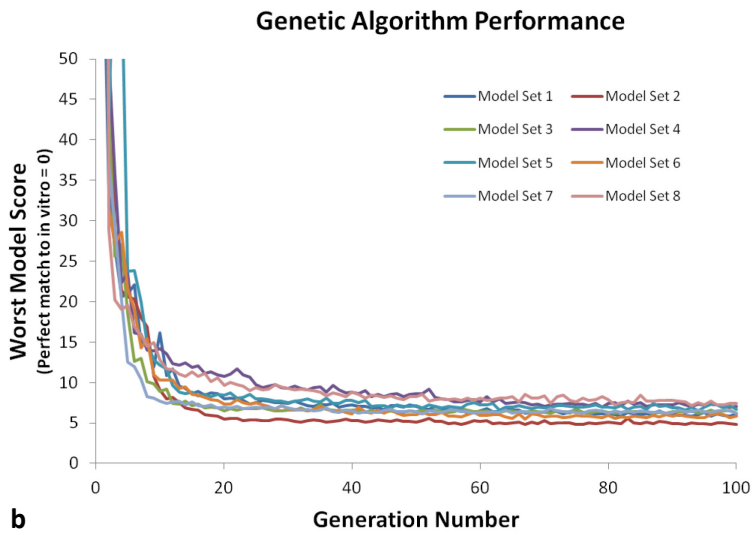
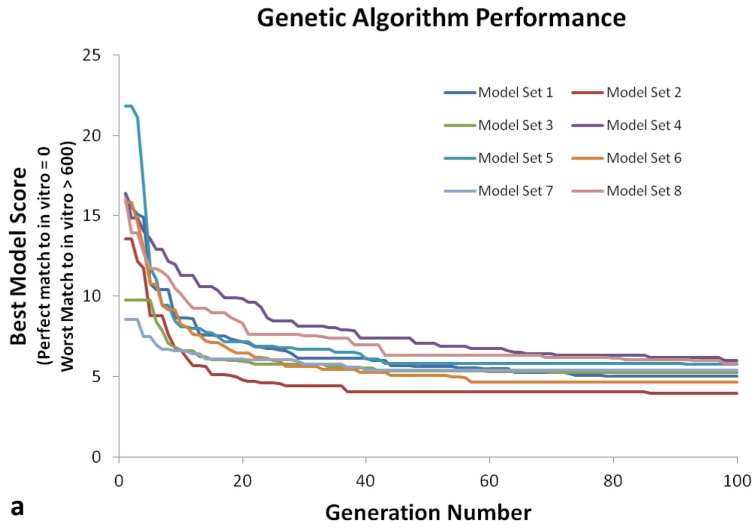
a

Actual Migration at Vegf 50 ng/ml

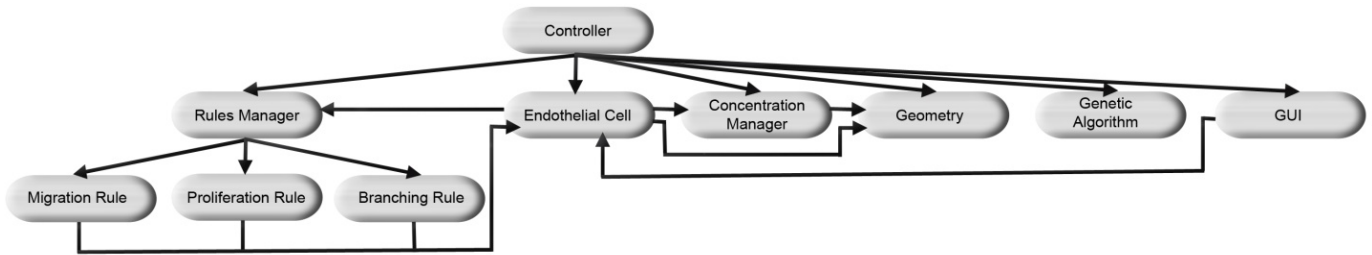


b

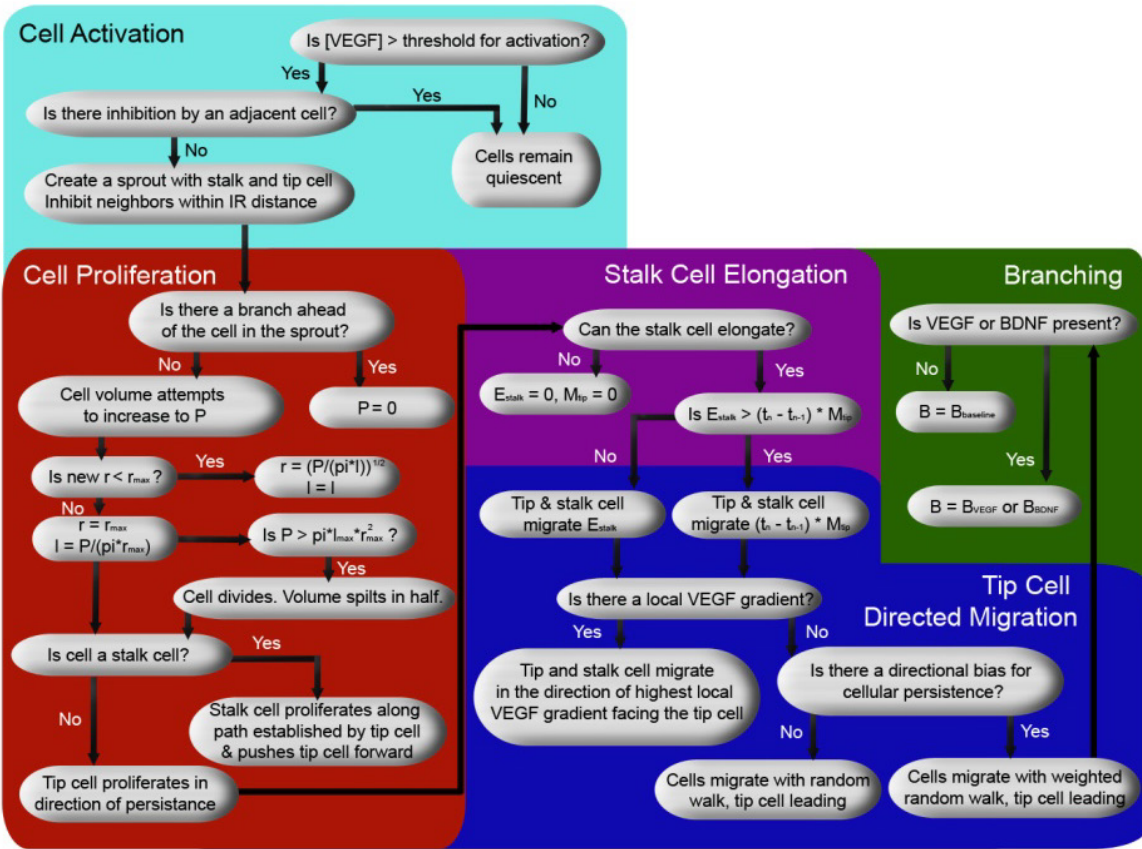
Supplementary Figure C.4.



Supplementary Figure C.5



a



b

Appendix D. Supplementary Tables

Supplementary Table D.1. Summary of cell behaviors modeled in discrete angiogenesis models that explicitly mention the order of behaviors.

Supplementary Table D.2. Migration parameters.

Supplementary Table D.3. Proliferation parameters.

Supplementary Table D.4. Branching parameters.

Supplementary Table D.5. Activation and morphological parameters.

Supplementary Table D.1.

Model Reference	Discrete Behaviors	Behavior Interactions
(Bauer et al., 2007; Bauer et al., 2009)	Mitosis, proliferation, migration	Cells have clocks to indicate place in cell cycle. Cells cannot proliferate and chemotactically move at the same time.
(Bentley et al., 2009; Jakobsson et al., 2010)	Filopodia retraction, Cell shuffling	Retraction starts after the top membrane agent has failed to extend for some number of consecutive time-steps. Cells shuffle (swap) positions with probabilities determined by active Notch level and VEGFR-2 receptor level.
(Chaplain, 2000)	Branching, mitosis	Branching is allowed after some threshold age when sufficient space is available. Cell division on an 18 hour cycle after 36-48 hours.
(Das et al., 2010)	Migration, proliferation, apoptosis	Transitions to the start of each cell behavior are probabilistic and functions of the cell's local environment
(Qutub and Popel, 2009)	Migration, proliferation, branching, elongation, phenotypic changes	All cells respond independently to a set of rules. Rules for the tip and stalk cells depend on each other: tip cell migration drives stalk cell elongation; stalk cell growth leads to tip cell migration
(Peirce and Skalak, 2003; Peirce et al., 2004)	Proliferation, differentiation, migration	Cells independently express select migration-promoting, proliferation-, and differentiation-regulating growth factors if a certain set of pre-defined conditions are met. Cell-cell contact stimulates differentiation.
(Thorne et al., 2011)	Proliferation, apoptosis, matrix production and degradation	Cells respond independently to a set of rules. Interactions are governed by growth factor production.
(Shirinifard et al., 2009)	Proliferation, migration	Vascular endothelial cell patterning defined by chemotaxis. Contact-inhibition defines neovascular growth.
(Merks et al., 2006)	Elongation, migration	Endothelial cell elongation is driven by cytoskeletal remodeling. Cells respond independently to a set of rules governing chemotaxis.
(Szabo et al., 2008)	Elongation, migration	Cells are preferentially guided toward adjacent elongated cells via a modified energy minimization (Cellular Potts) model.
(Milde et al., 2008)	Migration, branching, anastomosis	Cells respond independently to chemotactic and haptotactic directional cues. Cell cycle enforces a refractor period between deterministic branching events.
(Merks and Glazier, 2006; Merks et al., 2008)	Migration, branching	Cells secrete chemoattractant to allow for auto-/inter-cellular signaling. Cell-cell contact inhibition allows for sprouting and vascular network organization.

Supplementary Table D.2.

Migration Parameters			
Name	Description	Value	Reference
m_{baseline}	Baseline cell migration speed (Equations 1,2A, 2B)	6.2 $\mu\text{m/hr}$	(Korff and Augustin, 1999; Rupp et al., 2004)
c_1	Cell migration constant (Equation 2A)	0.1894 ml/ng	(Nakashio et al., 2002; Noiri et al., 1998; Wilson et al., 2006; Yamaguchi et al., 1999)
c_2	Cell migration constant (Equation 2B)	1.863 1/ln(ng/ml)	(Dimmeler et al., 2000)
c_3	Cell migration constant (Equation 2B)	137.4	(Dimmeler et al., 2000)
$\text{max}_{\text{migration}}$	Maximum total migration speed (Equation 1)	40 $\mu\text{m/hr}$	(Stokes et al., 1991)
w_{pers}	Weight of persistence vector (Equation 3)	3	Approximates observed <i>in vitro</i> tortuosity
w_{grad}	Weight of VEGF gradient (Equation 3)	1	Approximates observed <i>in vitro</i> tortuosity
w_{rand}	Weight of random vector (Equation 3)	.05	Approximates observed <i>in vitro</i> tortuosity
θ_{mig}	Maximum deviation of migration	90°	Prevents backwards turns

Supplementary Table D.3.

Proliferation Parameters			
Name	Description	Value	Reference
r_1	Cell VEGF growth rate (Equation 4A)	0.032577 ml/ng	(McLaughlin and De Vries, 2001; Wilson et al., 2006; Wu et al., 2006; Wu et al., 2000)
r_2	Cell growth BDNF threshold (Equation 4A)	0 ng/ml	Estimated from in vitro observations
r_3	Cell BDNF growth rate (Equation 4A)	0	Estimated from in vitro observations
r_4	Cell BDNF growth rate (Equation 4A)	1	Estimated from in vitro observations
g_{baseline}	Baseline cell growth rate (Equation 4A)	0.027676 1/hr	(Varma et al., 2005)
n_{active}	Fraction of cells within a group actively proliferating at any moment (Equation 4B)	.12	(Bachetti et al., 2004)
len_{min}	Minimum possible (proportioned) cell length for mitosis	20 μm	(Neufeld et al., 1986)
r_5	Mitosis probability constant (Equation 5)	0.012617 1/ μm	(Neufeld et al., 1986)
r_6	Mitosis probability constant (Equation 5)	-0.13738	(Neufeld et al., 1986)
f_{branch}	Extra branch proliferation factor for constant action models	4	Selected to approximate <i>in vitro</i> preliminary branch length data
p_{branch}	Forced branch proliferation probability for state machine models	0.75	Selected to approximate <i>in vitro</i> preliminary branch length data
t_{branch}	Time that f_{branch} and p_{branch} are in effect for a branch after it is created	10 hours	Selected to approximate <i>in vitro</i> preliminary branch length data

Supplementary Table D.4.

Branching Parameters			
Name	Description	Value	Reference
θ_{\max}	Maximum cell branching angle	90°	Prevents backwards branches
θ_{\min}	Minimum cell branching angle	9°	Estimated as 1/10 th of maximum; avoids cell overlap
b_1	VEGF threshold for cell branching probability b_3 (Equation 6)	0 ng/ml	Estimated from in vitro observations
b_2	BDNF threshold for cell branching probability b_3 (Equation 6)	0 ng/ml	Estimated from in vitro observations
b_3	Cell branching probability above VEGF or BDNF threshold (Equation 6)	0.1	Estimated from in vitro observations
b_4	Cell branching probability at or below VEGF and BDNF thresholds (Equation 6)	0.05	Approximates <i>in vitro</i> branching of control case

Supplementary Table D.5.

Activation and Morphological Parameters			
Name	Description	Value	Reference
act_{VEGF_X}	Probability of an endothelial cell on the surface of the embedded spheroid becoming activated due to local VEGF concentration during a 1 hour period when $[VEGF] = X$ ng/ml (Eqn. 7)	When $X = 0$ ng/ml, 0.01 When $X = 25$ ng/ml, 0.90	Estimated from in vitro observations
act_{BDNF_X}	Probability of a cluster endothelial cell becoming activated due to local BDNF concentration during a 1 hour period when $[BDNF] = X$ ng/ml (Eqn. 7)	When $X = 0$ ng/ml, 0.01 When $X = 25$ ng/ml, 0.90	Estimated from in vitro observations, assumed identical to VEGF activation
len_{tip}	Initial tip cell length	10 μ m	Estimated from in vitro observations
len_{stalk}	Initial stalk cell length	10 μ m	Estimated from in vitro observations
r_{init}	Initial sprout radius	4 μ m	Approximation of base width of smallest discernible <i>in vitro</i> sprout at 6 hours
$r_{inhibit}$	Radius of inhibition of an activated cell	3 cells	Approximates observed <i>in vitro</i> sprout count
$d_{spheroid}$	Diameter of initial spheroid cluster of cells	120 μ m	Selected from our own spheroids
d_{sphere}	Diameter of each spherical cell in spheroid	13 μ m	(Korff and Augustin, 1998)
l_b	Length of new branch cells	7 μ m	At 6 hours 26% of all <i>in vitro</i> branches had lengths of less than 7 microns
r_b	Radius of new branch cells	1 μ m	Approximation of narrowest discernible <i>in vitro</i> branch width at 6

			hours
q_{\min}	Minimum sprout cell length-to-width ratio (Equation 8)	1	Assumption that a cell will orient itself along its sprout
q_{\max}	Maximum sprout cell length-to-width ratio (Equation 8)	4.5	(Yu et al., 1997)
q_{dist}	Minimum to maximum sprout cell length-to-width transition distance (Equation 8)	5 cells	Approximate maximum of longest observed <i>in vitro</i> sprout
e	Maximum stalk cell elongation factor	0.2	(Wang et al., 2003)

Supplementary References

- Bachetti, T., Comini, L., Francolini, G., Bastianon, D., Valetti, B., Cadei, M., Grigolato, P., Suzuki, H., Finazzi, D., Albertini, A., Curello, S., Ferrari, R., 2004. Arginase pathway in human endothelial cells in pathophysiological conditions. *Journal of Molecular and Cellular Cardiology* 37, 515-523, doi:10.1016/j.yjmcc.2004.05.004.
- Bauer, A. L., Jackson, T. L., Jiang, Y., 2007. A cell-based model exhibiting branching and anastomosis during tumor-induced angiogenesis. *Biophys J* 92, 3105-21.
- Bauer, A. L., Jackson, T. L., Jiang, Y., 2009. Topography of extracellular matrix mediates vascular morphogenesis and migration speeds in angiogenesis. *PLoS Comput Biol* 5, e1000445.
- Bentley, K., Mariggi, G., Gerhardt, H., Bates, P. A., 2009. Tipping the balance: robustness of tip cell selection, migration and fusion in angiogenesis. *PLoS Comput Biol* 5, e1000549.
- Chaplain, M. A. J., 2000. Mathematical modelling of angiogenesis. *Journal of Neuro-Oncology* 50, 37-51.
- Das, A., Lauffenburger, D., Asada, H., Kamm, R. D., 2010. A hybrid continuum-discrete modelling approach to predict and control angiogenesis: analysis of combinatorial growth factor and matrix effects on vessel-sprouting morphology. *Philos Transact A Math Phys Eng Sci* 368, 2937-60.
- Dimmeler, S., Dernbach, E., Zeiher, A. M., 2000. Phosphorylation of the endothelial nitric oxide synthase at Ser-1177 is required for VEGF-induced endothelial cell migration. *FEBS letters* 477, 258-262.
- Hu, Y., Wang, Y.-d., Guo, T., Wei, W.-n., Sun, C.-y., Zhang, L., Huang, J., 2007. Identification of brain-derived neurotrophic factor as a novel angiogenic protein in multiple myeloma. *Cancer genetics and cytogenetics* 178, 1-10.
- Jakobsson, L., Franco, C. A., Bentley, K., Collins, R. T., Ponsioen, B., Aspalter, I. M., Rosewell, I., Busse, M., Thurston, G., Medvinsky, A., Schulte-Merker, S., Gerhardt, H., 2010. Endothelial cells dynamically compete for the tip cell position during angiogenic sprouting. *Nat Cell Biol* 12, 943-53.
- Kermani, P., Rafii, D., Jin, D. K., Whitlock, P., Schaffer, W., Chiang, A., Vincent, L., Friedrich, M., Shido, K., Hackett, N. R., Crystal, R. G., Rafii, S., Hempstead, B. L., 2005. Neurotrophins promote revascularization by local recruitment of TrkB+ endothelial cells and systemic mobilization of hematopoietic progenitors. *The Journal of Clinical Investigation* 115, 653-663, doi:10.1172/jci22655.
- Kim, H., Li, Q., Hempstead, B. L., Madri, J. A., 2004. Paracrine and Autocrine Functions of Brain-derived Neurotrophic Factor (BDNF) and Nerve Growth Factor (NGF) in Brain-derived Endothelial Cells. *Journal of Biological Chemistry* 279, 33538-33546, doi:10.1074/jbc.M404115200.
- Korff, T., Augustin, H. G., 1998. Integration of endothelial cells in multicellular spheroids prevents apoptosis and induces differentiation. *J Cell Biol* 143, 1341-52.
- Korff, T., Augustin, H. G., 1999. Tensional forces in fibrillar extracellular matrices control directional capillary sprouting. *J Cell Sci* 112 (Pt 19), 3249-58.
- Lam, C.-T., Yang, Z.-F., Lau, C.-K., Tam, K.-H., Fan, S.-T., Poon, R. T. P., 2011. Brain-Derived Neurotrophic Factor Promotes Tumorigenesis via Induction of Neovascularization: Implication in Hepatocellular Carcinoma. *Clinical Cancer Research* 17, 3123-3133, doi:10.1158/1078-0432.ccr-10-2802.
- McLaughlin, A. P., De Vries, G. W., 2001. Role of PLCgamma and Ca(2+) in VEGF- and FGF-induced choroidal endothelial cell proliferation. *Am J Physiol Cell Physiol* 281, C1448-56.
- Merks, R. M., Glazier, J. A., 2006. Dynamic mechanisms of blood vessel growth. *Nonlinearity* 19, C1-C10, doi:10.1088/0951-7715/19/1/000.
- Merks, R. M., Perryn, E. D., Shirinifard, A., Glazier, J. A., 2008. Contact-inhibited chemotaxis in de novo and sprouting blood-vessel growth. *PLoS Comput Biol* 4, e1000163.

- Merks, R. M., Brodsky, S. V., Goligorsky, M. S., Newman, S. A., Glazier, J. A., 2006. Cell elongation is key to in silico replication of in vitro vasculogenesis and subsequent remodeling. *Dev Biol* 289, 44-54.
- Milde, F., Bergdorf, M., Koumoutsakos, P., 2008. A hybrid model for three-dimensional simulations of sprouting angiogenesis. *Biophys J* 95, 3146-60, doi:10.1529/biophysj.107.124511.
- Nakashio, A., Fujita, N., Tsuruo, T., 2002. Topotecan inhibits VEGF- and bFGF-induced vascular endothelial cell migration via downregulation of the PI3K-Akt signaling pathway. *Int J Cancer* 98, 36-41.
- Neufeld, A. H., Jumblatt, M. M., Matkin, E. D., Raymond, G. M., 1986. Maintenance of corneal endothelial cell shape by prostaglandin E2: effects of EGF and indomethacin. *Invest Ophthalmol Vis Sci* 27, 1437-42.
- Noiri, E., Lee, E., Testa, J., Quigley, J., Colflesh, D., Keese, C. R., Giaever, I., Goligorsky, M. S., 1998. Podokinesis in endothelial cell migration: role of nitric oxide. *Am J Physiol* 274, C236-44.
- Peirce, S. M., Skalak, T. C., 2003. Microvascular remodeling: a complex continuum spanning angiogenesis to arteriogenesis. *Microcirculation* 10, 99-111.
- Peirce, S. M., Van Gieson, E. J., Skalak, T. C., 2004. Multicellular simulation predicts microvascular patterning and in silico tissue assembly. *Faseb J* 18, 731-3.
- Qutub, A. A., Popel, A. S., 2009. Elongation, proliferation & migration differentiate endothelial cell phenotypes and determine capillary sprouting. *BMC Syst Biol* 3, 13.
- Rupp, P. A., Czirok, A., Little, C. D., 2004. α v β 3 integrin-dependent endothelial cell dynamics in vivo. *Development* 131, 2887-97.
- Shirinifard, A., Gens, J. S., Zaitlen, B. L., Poplawski, N. J., Swat, M., Glazier, J. A., 2009. 3D multi-cell simulation of tumor growth and angiogenesis. *PLoS ONE* 4, e7190.
- Stokes, C. L., Lauffenburger, D. A., Williams, S. K., 1991. Migration of individual microvessel endothelial cells: stochastic model and parameter measurement. *J Cell Sci* 99 (Pt 2), 419-30.
- Szabo, A., Mehes, E., Kosa, E., Czirok, A., 2008. Multicellular sprouting in vitro. *Biophys J* 95, 2702-10, doi:10.1529/biophysj.108.129668.
- Thorne, B. C., Hayenga, H. N., Humphrey, J. D., Peirce, S. M., 2011. Toward a multi-scale computational model of arterial adaptation in hypertension: verification of a multi-cell agent based model. *Front Physiol* 2, 20, doi:10.3389/fphys.2011.00020.
- Varma, S., Lal, B. K., Zheng, R., Breslin, J. W., Saito, S., Pappas, P. J., Robert W. Hobson, I., Durán, W. N., 2005. Hyperglycemia alters PI3k and Akt signaling and leads to endothelial cell proliferative dysfunction. *American Journal of Physiology – Heart and Circulatory Physiology* 289, H1744-H1751.
- Verhulst, P. F., 1838. Notice sur la loi que la population suit dans son accroissement. *Corres. Math. et Physique* 10, 113-121, doi:citeulike-article-id:2142779.
- Wang, B. W., Chang, H., Lin, S., Kuan, P., Shyu, K. G., 2003. Induction of matrix metalloproteinases-14 and -2 by cyclical mechanical stretch is mediated by tumor necrosis factor- α in cultured human umbilical vein endothelial cells. *Cardiovasc Res* 59, 460-9.
- Whitley, D., 1994. A genetic algorithm tutorial. *Statistics and Computing* 4, 65-85, doi:10.1007/bf00175354.
- Wilson, B. D., Li, M., Park, K. W., Suli, A., Sorensen, L. K., Larriue-Lahargue, F., Urness, L. D., Suh, W., Asai, J., Kock, G. A., Thorne, T., Silver, M., Thomas, K. R., Chien, C. B., Losordo, D. W., Li, D. Y., 2006. Netrins promote developmental and therapeutic angiogenesis. *Science* 313, 640-4.
- Wu, G., Luo, J., Rana, J. S., Laham, R., Sellke, F. W., Li, J., 2006. Involvement of COX-2 in VEGF-induced angiogenesis via P38 and JNK pathways in vascular endothelial cells. *Cardiovascular Research* 69, 512-519, doi:10.1016/j.cardiores.2005.09.019.

- Wu, L.-W., Mayo, L. D., Dunbar, J. D., Kessler, K. M., Baerwald, M. R., Jaffe, E. A., Wang, D., Warren, R. S., Donner, D. B., 2000. Utilization of Distinct Signaling Pathways by Receptors for Vascular Endothelial Cell Growth Factor and Other Mitogens in the Induction of Endothelial Cell Proliferation. *The Journal of Biological Chemistry* 275, 5096-5103.
- Yamaguchi, N., Anand-Apte, B., Lee, M., Sasaki, T., Fukai, N., Shapiro, R., Que, I., Lowik, C., Timpl, R., Olsen, B. R., 1999. Endostatin inhibits VEGF-induced endothelial cell migration and tumor growth independently of zinc binding. *Embo J* 18, 4414-23.
- Yu, P. K., Yu, D., Alder, V. A., Seydel, U., Su, E., Cringle, S. J., 1997. Heterogeneous endothelial cell structure along the porcine retinal microvasculature. *Exp Eye Res* 65, 379-89.